This is a preprint, the final version is subject to change, of the American Mineralogist (MSA)
Cite as Authors (Year) Title. American Mineralogist, in press.
DOI: https://doi.org/10.2138/am-2019-6786

Revision 1

Role of micropores, mass transfer, and reaction rate in the hydrothermal alteration process of plagioclase in a granitic pluton.

Takashi Yuguchi [1]*, Kaho Shoubuzawa [1], Yasuhiro Ogita [1], Koshi Yagi [2], Masayuki Ishibashi [3], Eiji Sasao [3], and Tadao Nishiyama [4]

[1] Faculty of Science, Yamagata University, 1-4-12 Kojirakawa, Yamagata 990-8560, Japan.

[2] Hiruzen Institute for Geology and Chronology Co., Ltd., 2-5, Nakashima, Naka-ku, Okayama 703-8252, Japan.

[3] Mizunami Underground Research Laboratory, Japan Atomic Energy Agency, 1-64, Yamanouchi, Akiyo, Mizunami, Gifu 509-6132, Japan.

[4] Department of Earth and Environmental Science, Faculty of Advanced Science and Technology, Kumamoto University, 2-39-1, Kurokami, Chuo-ku, Kumamoto 860-8555, Japan.

* Corresponding author: T. Yuguchi

E-mail address: takashi_yuguchi@sci.kj.yamagata-u.ac.jp

Tel: +81 23 628 4641 / Fax: +81 23 628 4661

This is a preprint, the final version is subject to change, of the American Mineralogist (MSA)
Cite as Authors (Year) Title. American Mineralogist, in press.
DOI: https://doi.org/10.2138/am-2019-6786

ABSTRACT

This paper describes the plagioclase alteration process with a focus on the role of micropores, mass transfer, and reaction rate in the Toki granitic pluton in central Japan. The plagioclase alteration process involves albitization, K-feldspathization, and the formation of illite, calcite, fluorite, and epidote, which is classified into three categories based on their distribution: overall alteration throughout the plagioclase grain (Type A), alteration at the cores of the grain, (Type B), and the partial alteration at the rims of the grain (Type C). Micropores form during the incipient stage of plagioclase alteration by dissolution of the anorthite component, and then contribute to the infiltration of hydrothermal fluid into the plagioclase, resulting in further progress of the alteration. The distribution of the micropores within the plagioclase is a key factor of the alteration, resulting in the Type A–C distribution patterns. Another factor in plagioclase alteration is the mass transfer of the components released from biotite by chloritization. The overall reactions lead to the quantitative assessment of mass transfer between the reactant and product minerals during the alteration: the alteration involves the inflow of H_4SiO_4, Al^{3+}, Fe^{2+}, Mn^{2+}, Mg^{2+}, K^+, CO_2 and F^-, and the outflow of H_2O, H^+, and Ca^{2+}. The age of the plagioclase alteration was determined to be 59.2 ± 1.4 Ma by illite K-Ar geochronology. The combination of this age and the time-temperature (*t*-*T*) path determined by thermochronometry yields a temperature range from 290 to 305 °C. Chronological data suggest that the serial alteration processes from biotite chloritization to plagioclase alteration occurred during 68–51 Ma and at a temperature of 180–350 °C within the rock body. The biotite chloritization and plagioclase alteration led to sequential

This is a preprint, the final version is subject to change, of the American Mineralogist (MSA)
Cite as Authors (Year) Title. American Mineralogist, in press.
DOI: https://doi.org/10.2138/am-2019-6786

variations in the fluid chemistry: the concentrations of aluminum, iron, manganese, and magnesium ions in the hydrothermal fluid decrease gradually, and the concentrations of calcium and fluorine ions in the fluid increase gradually as the biotite chloritization and plagioclase alteration proceed. Both processes also cause variations in the pH of the hydrothermal fluid that affect the dissolution of plagioclase. The infiltration rate of the hydrothermal fluid (HFI rate) and the potassium transfer rate (KT rate) through the micropores into the plagioclase represent the mass transfer rate of the alteration: the maximum HFI rate ranges from 38.0×10^{-6} to 68.1×10^{-6} μm/year and the maximum KT rate ranges from 36.3×10^{-6} to 64.1×10^{-6} μm/year. These rates can be used to determine the rate of the plagioclase alteration reaction, which ranges from 9.25×10^{-13} to 3.45×10^{-12} gram atom oxygen cm^{-2} s^{-1}. The mass transfer rate and reaction rate are possible indicators that relate the extent of hydrothermal alteration in the plagioclase to the time scale.

Keywords: Hydrothermal alteration; Micropores; Mass transfer; Albitization; Illite K-Ar age; Toki granitic pluton.

This is a preprint, the final version is subject to change, of the American Mineralogist (MSA)
Cite as Authors (Year) Title. American Mineralogist, in press.
DOI: https://doi.org/10.2138/am-2019-6786

INTRODUCTION

This study focuses on the hydrothermal alteration process of plagioclase in a granitic pluton. The degree and extent of hydrothermal alteration in a granitic rock have a significant effect on its weathering processes, which also influence the chemical characteristics of the groundwater due to water–rock interactions. Future forecasting of the geochemical features of a granitic rock contributes to safety evaluations of the geological disposal of nuclear waste and the geological storage of oil and natural gas; e.g., it can be predicted whether oxidative fluid (groundwater) will cause the corrosion of artificial metal objects in the facilities. Understanding the long-term history of the chemical characteristics of the hydrothermal fluid and groundwater within a pluton is, therefore, an important subject for such forecasts.

The hydrothermal alteration of granitic rock is constrained mainly by the dissolution–precipitation process during the infiltration of hydrothermal fluid along microcracks and through micropores (Nishimoto and Yoshida 2010). In this hydrothermal alteration process, plagioclase alteration occurs ubiquitously throughout a granitic body at temperatures below 400 °C (e.g. Ferry 1979; Boulvais et al. 2007). The secondary minerals of hydrothermal origin in plagioclase provide a record of the chemical characteristics of the hydrothermal fluid (Yuguchi et al. 2015), and thus, understanding the plagioclase alteration will therefore provide an understanding of the nature of the fluid chemistry of the entire pluton.

Plagioclase alteration is closely related to biotite chloritization (Eliasson 1993). Biotite chloritization also occurs ubiquitously throughout a granitic body at temperatures below

400 °C (e.g., Cathelineau 1988; Yoneda and Maeda 2008). The chemical nature of the biotite chloritization and plagioclase alteration processes, their temporal and thermal conditions, and their connections via microcracks and/or micropores provide significant clues regarding the nature of the sequential and long-term variations in fluid chemistry and mass transfer due to hydrothermal fluid advection in a granitic pluton throughout a wide temperature range during sub-solidus cooling. The chemical characteristics relating the reaction and temperature conditions of biotite chloritization have already been reported by Yuguchi et al. (2015). This paper describes 1) the nature of the micropores in the plagioclase, such as their distribution and volume, in order to evaluate the transfer pathways of the chemical components, 2) the nature of the plagioclase alteration reaction, as inferred by petrography and mineral chemistry, 3) the physical conditions, including the alteration age and the corresponding temperature, as estimated by illite K-Ar geochronology, 4) the sequential variations in the fluid chemistry, and 5) the possible indicators representing the mass transfer rate and reaction rate of plagioclase alteration, taking the Toki granite in the Tono district, central Japan, as an example. The Toki granite has two vertical shafts about 500 m long (see Sampling and Analytical Procedures), allowing us to collect samples from deep within the pluton. These samples have escaped weathering and are suitable for the study of plagioclase alteration.

The plagioclase alteration of granitic rocks gives information about the mass transfer among the reactants, products, and hydrothermal fluid, as has been described in previous studies (e.g. Ferry 1979; Plümper and Putnis 2009; Morad et al. 2010). These studies did not take the relationship between the volumes of the reactants and products into account when

deriving the reactions. This paper focuses on the role of micropores, which enhance mass transfer, in the alteration process by considering this volume relationship. We will then derive reactions leading to plagioclase alteration that are consistent with the volume relationship between the reactants and products.

Yuguchi et al. (2018) presented the position-specific time-temperature (*t*-*T*) paths of fifteen samples within the Toki granite, which are effective tools for determining both the temporal and thermal conditions of the secondary minerals. The chemical composition of chlorite can reveal the formation temperature through the chlorite thermometer effect (Yuguchi et al. 2015). K-Ar geochronology can provide the formation ages of mica clay minerals such as illite and sericite through hydrothermal alteration; illite occurs within the altered plagioclase in this study. Although the biotite chloritization and plagioclase illitization in the Toki granite occurred by a serial alteration process during the infiltration of hydrothermal fluid (Nishimoto et al. 2008; Nishimoto and Yoshida 2010), the age of illite and the formation temperature of chlorite are independent indicators of alteration. However, the *t*-*T* path of the sampling site can give both the age and temperature of formation simultaneously; the age (or temperature) of the secondary mineral will give the corresponding temperature (or age) through the *t*-*T* path. Therefore, the physical (thermal and temporal) conditions of the biotite chloritization and plagioclase alteration can be established, enabling us to discuss the sequential variations in the fluid chemistry and mass transfer. Furthermore, the determination of the temporal properties of the alteration phenomena allows us to discuss the mass transfer rate and reaction rate of the plagioclase alteration.

This is a preprint, the final version is subject to change, of the American Mineralogist (MSA)
Cite as Authors (Year) Title. American Mineralogist, in press.
DOI: https://doi.org/10.2138/am-2019-6786

THE TOKI GRANITE

Late Cretaceous granitic rocks are widely distributed throughout the Inner Zone (northern side of the Median Tectonic Line) of the Southwest Japan Arc, occurring in the parallel, east–west oriented Ryoke, Sanyo, and San-in Belts (Ishihara 2003). The Toki granite in the Tono district, central Japan, is one of the Late Cretaceous plutonic bodies of the Sanyo Belt (Fig. 1A: Ishihara and Chappell 2007). The Toki granite is a stock about 14 × 12 km^2 in area (Ishihara and Suzuki 1969) that intrudes into the Jurassic sedimentary rocks of the Kamiaso unit in the Mino Terrane (Sano et al. 1992) as well as into the late Cretaceous Nohi rhyolite (Sonehara and Harayama 2007) (Fig. 1B). A whole-rock Rb–Sr isochron age of 72.3 ± 3.9 Ma and a monazite chemical Th-U-total Pb isochron (CHIME) age of 68.3 ± 1.8 Ma were reported by Shibata and Ishihara (1979) and Suzuki and Adachi (1998), respectively. The Toki granite has zircon U–Pb ages of 74.7 ± 4.2 to 70.4 ± 1.7 Ma, which correspond to the time period from its incipient intrusion into the shallow crust through emplacement to the crystallization/solidification of the granite pluton (Yuguchi et al. 2016). Yuguchi et al. (2011C) presented that the Toki granite has hornblende K–Ar ages of 74.3 ± 3.7 Ma with a closure temperature of 510 ± 25 °C (Dodson and McClelland-Brown 1985), biotite K–Ar ages of 78.5 ± 3.9 to 59.7 ± 1.5 Ma (N = 33) with a closure temperature of 350–400 °C (Grove and Harrison 1996), and zircon fission-track (ZFT) ages of 75.6 ± 3.3 to 52.8 ± 2.6 Ma (N = 44) with a partial annealing zone (PAZ) of 190–350 °C. Yuguchi et al. (2017) also reported apatite fission-track (AFT) ages ranging from 52.1 ± 2.8 to 37.1 ± 3.6 Ma (N = 33) with a PAZ of 60–120 °C. On the basis of phase relationships, Yamasaki and Umeda (2012)

estimated that the emplacement depth of the granitic magma was about 5–7 km below the surface. The Toki granite is overlain unconformably by the Miocene Mizunami Group and the Mio-Pleistocene Tokai Group (Itoigawa 1974, 1980; Todo Collaborative Research Group 1999).

A series of studies by the authors have described the formation processes of the Toki granitic pluton from intrusion through emplacement to cooling (Yuguchi et al. 2010, 2011A, 2011B, 2011C, 2013, 2015, 2016, 2017, 2018). The Toki granite, a zoned pluton, has three rock facies grading from muscovite-biotite granite (MBG) at the margin through hornblende-biotite granite (HBG) to biotite granite (BG) in the interior (Fig. 1C). The boundaries of the three rock facies are defined by the appearance (MBG/HBG) and disappearance (HBG/BG) of hornblende without a chilled margin (Yuguchi et al. 2010). The geology and petrography of the Toki granite were described in detail by Yuguchi et al. (2010, 2011A, 2011B), and a description of the hydrothermal alteration in the Toki granite was given by Nishimoto et al. (2008), Nishimoto and Yoshida (2010), Ishibashi et al. (2014), Yuguchi et al. (2015) and Ishibashi et al. (2016).

This is a preprint, the final version is subject to change, of the American Mineralogist (MSA)
Cite as Authors (Year) Title. American Mineralogist, in press.
DOI: https://doi.org/10.2138/am-2019-6786

SAMPLING AND ANALYTICAL PROCEDURES

The Mizunami Underground Research Laboratory, consisting of two vertical shafts (the main and ventilation shafts), horizontal tunnels (sub-stages connecting the two shafts at intervals of 100 m from the ground level, with measurement niches at the 200 m and 300 m levels and access/research galleries at the 300 m and 500 m levels), is located on the sedimentary Mizunami Group, which unconformably overlies the Toki granite (Fig. 1B, D and E). Both the main and ventilation shafts are 500 m deep, ranging from an altitude of 201 masl (meters above sea level) (ground level) to an altitude of -299 masl (shaft bottom) (Fig. 1E). The unconformity between the Mizunami Group and the Toki granite is intersected by the shafts at a depth of about 170 m. This study employed borehole 06MI03 (vertical and 336 m long). The borehole was drilled from an underground depth of 191 m in the ventilation shaft before excavation was continued at depths below 191 m (Fig. 1E). Yuguchi et al. (2015) discussed the petrography, chemistry, and mass transfer of biotite chloritization in rock samples collected from the rock mass at a depth of around 500 m (altitude: -299 masl) in the ventilation shaft (Fig. 1E). This study employed the same samples, which originated from the deepest part of borehole 06MI03 in the altitude range of -274 masl to -314 masl (9 samples spaced 5 meters apart) (Fig. 1E). A restricted sampling range has the merit of providing rock samples that underwent the same temperature and pressure history during the sub-solidus cooling process of the Toki granite.

The petrographical data in this study were obtained from two-dimensional thin sections. The thin section were produced carefully in order to prevent the partial losses of minerals.

Backscattered electron (BSE) images and chemical maps showing the elemental Si, Al, Ca, Na, and K concentrations were collected using a JEOL IT100A scanning electron microscope with an energy-dispersive X-ray spectrometer (EDS) installed at Yamagata University, operating at an accelerating voltage of 15 kV and a beam current of 1.5 nA. Minerals were analyzed using an electron microprobe analyzer (JEOL JXA-8900) with a wavelength-dispersive X-ray spectrometer (WDS) housed at Yamagata University. The analytical conditions for quantitative analysis were an acceleration voltage of 15 kV, a beam current of 20 nA, a beam diameter of 3 μm, and the ZAF data correction method. The oxides and minerals which have known compositions were used as standard materials for quantitative determinations of mineral concentrations. The distribution of microcracks and micropores was determined using image processing software.

The illite from plagioclase alteration in sample No. 06MI03-8 was dated using K-Ar geochronology. The technique of Yagi (2006) and Yagi and Itaya (2011), which involves separation of plagioclase from the rock sample followed by separation of the illite from the plagioclase, yielded an illite powder with a diameter of 0.2–2.0 μm (see Appendix A). The composition of the separated illite was confirmed crystallographically using an X–ray powder diffractometer (Rigaku RINT–2500V) with a generation voltage of 40 kV and current of 160 mA, 0.5° divergence and scatter slits, and a 0.15 mm receiving slit. The profile was taken with a 2θ range from 2° to 40° using a step interval of 0.02° and a count time of 0.15 seconds per step. An oriented air-dried sample of 0.2–2.0 μm powder (10 mg) was scanned, as well as a sample of the >2.0 μm grain-size fraction that was identified in the control experiment. Further treatment with ethylene glycol, glycol cation exchange, and heating

(50 °C, 1 h) was employed for precise identification of the clay mineral. The mineral separation and XRD analysis were carried out at the Hiruzen Institute for Geology and Chronology Co. Ltd (Yagi 2006 and Yagi and Itaya 2011).

The radiogenic argon concentrations were analyzed with an isotope dilution mass spectrometer (HIRU, housed at the Research Institute of Natural Sciences, Okayama University of Science) following the technique of Itaya et al. (1991). Potassium was determined using flame photometry (HITACHI 180-30, housed at the Research Institute of Natural Sciences, Okayama University of Science) utilizing an internal standard as described by Nagao et al. (1984). The isotopic ages of the samples were calculated using the standard K-Ar age equation (Dalrymple and Lanphere 1969; Nagao and Itaya 1988; Dalrymple et al. 1999) with $\lambda_{\varepsilon} = 0.581 \times 10^{-10}$/year, $\lambda_{\beta} = 4.962 \times 10^{-10}$/year, and the $^{40}K/K$ value of 1.167×10^{-4} given by Steiger and Jäger (1977). The analytical uncertainties associated with the age determination were calculated using the method of Nagao and Itaya (1988).

This is a preprint, the final version is subject to change, of the American Mineralogist (MSA)
Cite as Authors (Year) Title. American Mineralogist, in press.
DOI: https://doi.org/10.2138/am-2019-6786

PETROGRAPHY

Sample descriptions

The mineral assemblage of the Toki granite consists of quartz, plagioclase, K-feldspar, biotite, hornblende, and muscovite, with accessory minerals including zircon, apatite, ilmenite, and magnetite and secondary minerals including chlorite, titanite, epidote, allanite, illite, and calcite. Plagioclase occurs as subhedral to euhedral crystals 1–20 mm across, ranging from 25 to 34 vol% in mode. Secondary alteration minerals are observed in most plagioclase. Equigranular quartz with crystals 0.5–25 mm across (20 to 33 vol%) and subhedral K-feldspar 1–12 mm across (27 to 41 vol%) are observed in the rock samples. The biotite has undergone variable degrees of alteration to become partially or wholly replaced by chlorite (Yuguchi et al. 2015). The volume of biotite ranges from 5 to 10 vol% and that of chlorite from 1 to 3 vol%. Fractures (microcracks) are distributed irregularly in the sample, and are frequently filled with calcite. The feldspars include micropores and sub-solidus textures such as myrmekite, reaction rim, and perthite (Yuguchi et al. 2011A, 2011B).

Unaltered plagioclase

The Toki granite contained both altered and unaltered plagioclase (1,893 plagioclase grains were observed in this study). About 6.8% (N = 128) of the unaltered plagioclase grains did not contain secondary minerals (Fig. 2A and 3). The unaltered plagioclase in Fig. 2A shows magmatic zonation ranging from $Ab_{77}An_{21}Or_2$ (core) to $Ab_{83}An_{15}Or_2$ (rim) with sub-solidus albite-rich reaction rims of $Ab_{98}An_1Or_1$ (Yuguchi et al. 2011A and B) (Fig. 4A).

This is a preprint, the final version is subject to change, of the American Mineralogist (MSA)
Cite as Authors (Year) Title. American Mineralogist, in press.
DOI: https://doi.org/10.2138/am-2019-6786

Plagioclase alteration

Plagioclase alteration in the Toki granite was classified into three categories based on the distribution pattern: overall alteration throughout the plagioclase grain (Type A, overall alteration: Fig. 2B), alteration of the core of the grain (Type B, core alteration: Fig. 2C), and partial alteration at the rims of the grain (Type C, rim alteration: Fig. 2D). Figure 3 shows a frequency diagram of Types A, B, and C in the observed plagioclase grains, demonstrating that about 93% of the plagioclase had experienced alteration. Type A, B, and C alterations were observed in about 29.8% (N = 565), 8.7% (N = 164), and 54.7% (N = 1,036), respectively, of the total number (N=1,893) of observed plagioclase grains.

Type A: Overall alteration throughout the plagioclase grain. Type A alteration is defined as the complete replacement of plagioclase by secondary alteration minerals, as shown in Fig. 2B. The altered area of the plagioclase, which includes albite, K-feldspar, illite, calcite, fluorite, and epidote, is shown in the BSE images (Fig. 4B) and chemical maps (Fig. S1A). Plagioclase alteration is always accompanied by albitization; additionally, formations of K-feldspar, illite, calcite, fluorite, and epidote (hereafter defined as associated minerals) can also occur. Type A is further subdivided into three sub-types (Types A-1 to A-3) based on the assemblage of mineral products (Figs. 2B and 4B; Table 1):

Type A-1: albite, K-feldspar, illite, and calcite products (sample No. 8-7: Figs. 4B-1 and S1A)

Type A-2: albite, illite, calcite, and fluorite products (No. 9-8: Fig. 4B-2)

Type A-3: albite, K-feldspar, fluorite, and epidote products (No. 12-7: Fig. 4B-3)

Albite is found throughout the plagioclase except at the sub-solidus reaction rim (myrmekite), and it formed a matrix that surrounded the associated minerals (Fig. 4B). The Type A samples varies in terms of the volume ratio between albite and the associated minerals, with both high ratios (Fig. 4B-1 and B-2) and low ratios (Fig. 4B-3) being observed. The chemical composition of albite ranges from Ab_{95} to Ab_{98} (Figs. 5A and S2; Table 2). Patchy-shaped K-feldspar occurs with a width of 10–200 μm (Figs. 4B-1 and S1A) and chemical composition ranging from Or_{87} to Or_{98} (Fig. 5A; Table 2). Calcite occurs with needle or columnar shapes less than 50 μm in width (Figs. 4B and S1A). Illite occurs with patchy shapes less than 80 μm in width with irregular boundaries (Fig. S1A). The chemical composition of illite is phengitic, and shows no significant changes among Types A, B, and C (Fig. 5B). Supplementary figure S3 shows the XRD pattern of the powder samples with a size range of 0.2–2.0 μm and those with a size >2.0 μm taken from the plagioclase of sample No. 06MI03-8, which confirmed the presence of illite crystallographically. Granular fluorite and epidote with sizes of up to 20 μm were observed in Type A-3 plagioclase alterations (Fig. 4B-3). The Type A-2 samples has a residual intact, i.e., unaltered, area in their cores (corresponding to the area that is a lighter gray than albite in the BSE image: Figs. 4B-3 and S1A-3), which demonstrates the magmatic composition of Ab_{87} (analysis No. J02: Table S1).

Type B: Alteration in the core of the plagioclase grain. Type B plagioclase alteration is defined by the partial replacement of the core of the plagioclase grain by alteration minerals, as shown in Fig. 2C. The alteration area is limited to the core in some samples (sample No.

12-2: Fig. 2C-1), and more widely distributed from the core to the rim in others (sample No. 7-8: Fig. 2C-2). The alteration area of the plagioclase, which includes albite, K-feldspar, illite, calcite, and fluorite, can be seen in the BSE images (Fig. 4C). Plagioclase alteration is accompanied essentially with albitization; formations of associated minerals may also occur. Type B alterations can be further subdivided into the following two sub-types based on the assemblage of product minerals (Table 1):

Type B-1: albite, K-feldspar, illite, calcite, and fluorite products (sample No. 12-2: Fig. 4C-1)

Type B-2: albite, K-feldspar, illite, and fluorite products (sample No. 7-8: Fig. 4C-2)

The chemical composition of albite ranges from Ab_{85} to Ab_{95} (Table 1 and S1), and it forms a matrix that surrounds the associated minerals (Fig. 4C). In sample No. 12-2, K-feldspar and illite show a mosaic-like texture (Fig. S1B). K-feldspar occurs as needle crystals less than 10 μm in width or as patchy crystals less than 100 μm in width, which ranges from Or_{94} to Or_{97} in chemical composition (Fig. 4C; Table 1). Illite occurs as patchy aggregates less than 60 μm in width with irregular boundaries (Figs. 4C, S1 and S2). Calcite occurs as patchy, columnar, or granular crystals less than 50 μm in length with irregular boundaries (Figs. 4Cand S1B). Fluorite occurs as granular crystals up to 20 μm across (Fig. S2). The composition of the intact plagioclase ranges from Ab_{71} to Ab_{76} (Table 1: analysis points J07 and J09) in contact with the alteration front (Fig. S2). The term “alteration front” signifies the boundary between the alteration area and the intact area, corresponding to the terminal position of the spread of the alteration.

Type C: Alteration of the rim of the plagioclase grain. Type C alteration involves the secondary alteration minerals partially replacing the plagioclase rims in contact with chloritized biotite as shown in Fig. 2D. The alteration fronts of the Type C samples shows irregular boundaries (Fig. 6A). This distribution indicates that the alteration progressed inward from the margin to the core, and that the alteration was related to biotite chloritization. The occurrence of the Type A (or B) alteration has a potential to be due to occasional observation of the surface perpendicular to the cutting plane showing the Type C alteration because thin sections were made from the samples cut in random orientation. This alteration is accompanied essentially with albitization; additionally, formations of associated minerals may occur. Type C alterations are further subdivided into the following three sub-types based on the assemblage of product minerals (Table 2):

Type C-1: albite, K-feldspar, calcite, and fluorite products (sample No. 6-6: Fig. 4D-1)

Type C-2: albite, K-feldspar, illite, and fluorite products (sample No. 6-9: Fig. 4D-2)

Type C-3: albite, K-feldspar, illite, calcite, and fluorite products (C-3-1: samples No. 7-6 of Fig. 4D-3, C-3-2: No. 9-4 of Fig. 4D-4 and C-3-3: No. 9-9 of Fig. 4D-5, which contain different volume ratios of the product minerals) (Table 2)

The chemical composition of albite ranges from Ab_{90} to Ab_{99} (Table 1 and S2), and it forms a matrix that surrounds the associated minerals (Fig. 4C). K-feldspar occurs as lamella less than 20 μm in width or as patchy zones less than 100 μm in width, and its chemical composition ranges from Or_{93} to Or_{97} (Table 1 and S2). Illite occurs as patchy zones less than 60 μm in width with irregular boundaries (Figs. 4D-4, 4D-5 and S2). K-feldspar and illite are aligned perpendicular with respect to the boundary between the altered plagioclase

This is a preprint, the final version is subject to change, of the American Mineralogist (MSA)
Cite as Authors (Year) Title. American Mineralogist, in press.
DOI: https://doi.org/10.2138/am-2019-6786

and the chloritized biotite (Fig. 4D-3). Calcite and fluorite occur as granular grains up to 20 μm across. The intact plagioclases that acted as the reactants for Type C alteration have chemical compositions ranging from Ab_{73} to Ab_{85} (Table 1 and S2). They were obtained from the analysis points (e.g., J13, 62, 76, J27, and 96) in contact with the alteration front (Fig. S2).

In sample No. 9-4, the alteration area branches irregularly in multiple directions, indicating a hydrothermal fluid channel structure (Figs. 4D-4 and 6B). The alteration (albitization) area of sample No. 9-4 also show a mottled distribution, in which the intact area is trapped in the alteration area (Fig. 6C), which also represents the channel structure of the hydrothermal fluid.

Micropores and microcracks

Both of the altered and intact areas include micropores (Fig. 6B and C) with columnar and granular shapes less than 15 μm in size along their major axis. The altered areas contained more micropores than the intact areas (Fig. 6B and C). Within the altered areas, albite and K-feldspar contained more micropores than illite, calcite, and fluorite (Fig. 6D and E).

Microcracks are also found in both the altered and intact areas (Fig. 6B). The microcracks cut across albite and K-feldspar, but not illite, calcite, or fluorite (Figs. 6B, C and S2). The volume of the micropores is larger than that of the microcracks (Fig. 8B).

Sub-solidus reaction rim

The albite-rich rims, such as myrmekite, and the reaction rim, which is referred to as the sub-

solidus reaction texture, are derived from sub-solidus deuteric alteration at a temperature below 500 °C (Yuguchi and Nishiyama 2008; Yuguchi et al. 2011A, 2011B). In the Toki granite, plagioclase rims in contact with K-feldspar are accompanied by sub-solidus reaction textures, but not by type A–C alterations (Fig. 8F). Micropores are frequently observed in the alteration area, but not in the sub-solidus reaction rim (Fig. 8F). Although type A–C alterations and the formation of sub-solidus reaction textures stem from the same albitization phenomena that occurred within the plagioclase at the sub-solidus stage, they had different mechanisms of formation and mass transfer.

This is a preprint, the final version is subject to change, of the American Mineralogist (MSA)
Cite as Authors (Year) Title. American Mineralogist, in press.
DOI: https://doi.org/10.2138/am-2019-6786

CHRONOLOGICAL RESULTS

The K-Ar dating results of the illite powder with a size range of 0.2–2.0 μm separated from the plagioclase of rock sample No. 06MI03-8 are shown in Table 3. The XRD pattern in Fig. S3 indicates that the powder used for dating includes not only illite, but also chlorite, plagioclase, quartz, and smectite. Of these minerals, only illite contains a significant amount of potassium (plagioclase contains less than 0.6 wt% potassium), and thus the other minerals did not influence the results of the K-Ar dating of illite. The 0.2–2.0 μm illite powder had a potassium concentration of 3.298 ± 0.066 wt%; the average of two quantitative values (3.3103 and 3.2856 wt%) was used for the age calculation. Multiple quantitative analyses of standard samples (JG-1 and JB-1) gave an error of less than 2% for the potassium concentration (Nagao et al. 1984), and thus the error of the potassium concentration for our sample was defined as 2%. Multiple runs of the standard sample (JG-1 biotite, 91 Ma) indicate an error of about 1% at the 2 sigma confidence level (Itaya et al. 1991; Yagi et al. 2015). Radiogenic ^{40}Ar (rad. ^{40}Ar) was present at 770.8 ± 10.0 × 10^{-8} cc STP/g (per unit mass (1 g) at the standard temperature (0 °C) and pressure (1 atm)); this value was obtained from the following equation on the basis of the ^{36}Ar, ^{38}Ar, and ^{40}Ar in the illite powder (Itaya et al. 1991): [rad. ^{40}Ar] = [sample ^{40}Ar] – [air ^{40}Ar] = [sample ^{40}Ar] – 295.5 × [sample ^{36}Ar]. The ratio of air contamination in ^{40}Ar (air contamination / non-rad. ^{40}Ar) was given as follows: {[sample ^{40}Ar] – [rad. ^{40}Ar]} / [sample ^{40}Ar] × 100 (%). Based on the results of the potassium concentration and radiogenic ^{40}Ar determination, the K-Ar age of the illite was calculated to be 59.2 ± 1.4 Ma.

This is a preprint, the final version is subject to change, of the American Mineralogist (MSA)
Cite as Authors (Year) Title. American Mineralogist, in press.
DOI: https://doi.org/10.2138/am-2019-6786

DISCUSSION

The role of micropores in plagioclase alteration

The area and volume fraction of the micropores in the alteration and intact areas were determined through analysis of images of the samples No. 6-10 (unaltered), 8-7 (Type A-1), 9-8 (Type A-2), 12-7 (Type A-3), 12-2 (Type B-1), 7-8 (Type B-2), 6-6 (Type C-1), 6-9 (Type C-2), 7-6 (Type C-3-1), 9-4 (Type C-3-2), and 9-9 (Type C-3-3). Details of the image analysis procedure using the image processing software Photoshop® and Scion image are illustrated in Fig. 7A and described in the figure caption. The volume fractions of micropores were estimated from their areal fractions by simply assuming the equivalence of areal and volume fractions (Yuguchi and Nishiyama 2008). The volume fractions of micropores in the alteration area are was larger than that in the intact area (Table 4). Sample No. 9-4 displays a hydrothermal fluid channel structure (Fig. 6B and 7B-1), which is also constrained by the distribution of the micropores because of the difference between the volume fraction of micropores in the alteration area (0.067: Fig. 7B-2) and the intact area (0.023: Fig. 7B-3). The alteration area, which consists of micropores (microcracks), albite, and the associated minerals, can be regarded as the 'hydrothermal fluid infiltration (HFI) area'. Figure 8 shows the relationship between the micropore area and the HFI area, which exhibits a high correlation (R^2 = 0.9957). Therefore, the micropores contributed to the infiltration of the hydrothermal fluid into the plagioclase; that is, the distribution of the micropores within the plagioclase is a contributing factor to the development of the Type A–C distribution patterns of plagioclase alteration.

This is a preprint, the final version is subject to change, of the American Mineralogist (MSA)
Cite as Authors (Year) Title. American Mineralogist, in press.
DOI: https://doi.org/10.2138/am-2019-6786

Figures 9 and S4 show BSE and binary images of the micropores in the alteration areas of samples No. 9-9 (Fig. 9), 7-6 (Fig. S4A), and 9-4 (Fig. S4B), giving the distribution of long axis direction of the micropores. In each sample, the long axis of the micropores is oriented toward chlorite. The long axis direction indicates the stretching direction of the micropore networks. That is, the micropores acted as pathway for the hydrothermal fluid and enhanced the mass transfer of the components released by biotite chloritization into the plagioclase (black arrows of Fig. 9 and S4), which is consistent with the sequential alteration processes from biotite chloritization to plagioclase alteration previously reported by Nishimoto et al. (2008) and Nishimoto and Yoshida (2010). The factors contributing to plagioclase alteration include not only the occurrence of micropores, and but also the components supplied by biotite chloritization. Plagioclase alteration cannot progress without these components, which results in the presence of intact areas regardless of the occurrence of micropores.

The formation of micropores was attributed essentially to the dissolution of calcium (anorthite component) from plagioclase (Nishimoto et al. 2008). Sample No. 9-4 has the highest volume fraction of micropores (0.067: Table 4) in the alteration area. A reconstruction of the original composition of plagioclase was carried out using the composition of albite ($Ab_{99}An_1$: J28 of Table S1) under the assumption that all the micropore volume was originally occupied by anorthitic plagioclase. This resulted in an original composition of $Ab_{93}An_7$ for sample No. 9-4, which is not consistent with the original magmatic composition ($Ab_{85}An_{13}$: J27 of Table S1). This indicates the preferential loss of the anorthite component from the plagioclase, in a quantity larger than the volumes of

micropores. Thus, micropores formed at the incipient stage of alteration by the dissolution of the anorthite component, and subsequently contributed to the infiltration of hydrothermal fluid inward into the plagioclase, resulting in further progress of the alteration process.

The long axis direction of micropores is consistent with the distribution pattern of the associated minerals (indicated by white arrows in the BSE images of Figs. 9 and S4). The widths of the associated minerals are greater than that of the micropores, indicating the micropores were expanded by the dissolution of adjacent plagioclase followed by the precipitation of the associated minerals. Albite and K-feldspar contain more micropores than illite, calcite, and fluorite (Fig. 6D and E). Therefore, the albitization and K-feldspathization occurred through solid-state replacement via exchange reactions such as $NaSiCa_{-1}Al_{-1}$ and $KSiCa_{-1}Al_{-1}$ within the plagioclase, whereas the formation of illite, calcite and fluorite occurred via the dissolution of plagioclase around the micropores and precipitation into the vacancies. That is, the plagioclase alteration process was a combination of 'solid-state replacement' and 'dissolution–precipitation' processes. The above observations provide an answer to the question of whether the alteration caused the formation of micropores or the micropores drove the alteration; both these phenomena occurred simultaneously during the plagioclase alteration process. Thus, the plagioclase alteration process presents a natural example of the dissolution–precipitation mechanism discussed by Putnis et al. (2007).

Plagioclase alteration reactions

The plagioclase alteration should be described by reaction equations that represent the

quantitative mass transfer between the reactant and product minerals and the inflow and outflow of components. To determine alteration reactions in such an open system, we must specify some conservation conditions. Even if the associated minerals precipitated into micropores (i.e., were sealed) within the plagioclase, the enlargement of the micropores due to dissolution indicates the possibility of volume reduction after alteration. It is difficult to evaluate the magnitude of volume reduction on the basis of petrographical observations. Thus, we will consider two extreme cases: 1) a constant volume process and 2) a process involving the maximum volume reduction from the reactants to the products. The maximum reduction in the volume is defined as the difference between the volume fraction of the micropores in the altered and intact areas (samples No. 9-8, 12-2, 7-8, 6-6, 6-9, 7-6, 9-4, and 9-9), or as the volume fraction of the micropores in the altered area in the absence of an intact area (samples No. 8-7 and 12-7) (Table 4). The actual phenomena can be assumed to lie between these two extreme cases. Two overall reaction equations for the extreme cases were constructed for each sub-type from Type A-1 to A-3, Type B-1 to B-2, and Type C-1 to C-3-3. We also considered the additional condition of the volume ratios of the product minerals in the alteration area in deriving the reaction equations (Table 2). Thus, alteration reactions that satisfy both the volume relationship between the reactants and products and the volume ratios of the product minerals were developed.

Formulation of the overall reaction: Type A-1 (sample No. 8-7: Pl → Ab + Kfs + Ill + Cal). The original composition of the reactant, plagioclase, in Type A samples is unknown because the plagioclase in Type A has been totally altered. Thus, the composition of the

This is a preprint, the final version is subject to change, of the American Mineralogist (MSA)
Cite as Authors (Year) Title. American Mineralogist, in press.
DOI: https://doi.org/10.2138/am-2019-6786

Type C plagioclase core was used as the Type A reactant composition. In Type A-1, the reactant is plagioclase (analysis No. 76 in Table 1; the analysis number corresponds to the location shown in Fig. S2) and the products are albite (No. O11), K-feldspar (No. O13), illite (No. 21), and calcite (ideal $CaCO_3$ is assumed). The molar volumes of the reactant and product minerals were derived from their chemical compositions (Table 1 and S1). The volume fractions of the product minerals are expressed as ratios, such as albite to K-feldspar to illite to calcite = 1:0.400:0.451:0.089 (Table 2). Details of the image analysis procedure giving the mineral ratio are illustrated in Fig. S5 and described in the figure caption. We considered the following reaction in an open system:

Pl + X = *a* Ab + *b* Kfs + *c* Ill + *d* Cal + Y (X and Y: open components)

where X denotes the influx of chemical components through an intergranular medium (hydrothermal fluid) and Y denotes the efflux from the system. Silicon species are represented by H_4SiO_4 in the reaction equation. The solution of a set of simultaneous equations was used to determine the stoichiometric coefficients *a, b, c, d* and *e* and those of the open components involved in X and Y. The simultaneous equations consisted of the conservations (1), (3), (4), and (5) below in the case of the constant volume alteration and the conservations (2), (3), (4) and (5) in case of the maximum volume reduction:

100.6626 = 100.3064 *a* + 108.6662 *b* + 134.8920 *c* + 36.9257 *d* (constant volume)…conservation (1)

100.6626 = 0.962 (100.3064 *a* + 108.6662 *b* + 134.8920 *c* + 36.9257 *d*) (maximum volume decrease of 3.8 vol%) …conservation (2)

b = 0.3692 *a* (volume relation between albite and K-feldspar: 1:0.400=100.3064*a*:

108.6662*b*) …conservation (3)

c = 0.3354 a (volume relation between albite and illite: 1:0.451=100.3064a:134.8920c) …conservation (4)

d = 0.2418 a (volume relation between albite and calcite: 1:0.089=100.3064a: 36.9257d) …conservation (5)

The numerical values in the conservation equations (1) and (2) denotes that molar volumes in each mineral (see footnote of Table 1). The conservations (1), (3), (4), and (5) give the following dehydration equation:

$Pl(Ab_{74}) + 0.444\ H_4SiO_4 + 0.125\ CO_2 + 0.447\ Al^{3+} + 0.015\ Fe^{2+} + 0.014\ Mg^{2+} + 0.386\ K^+ + 0.007F^- \rightarrow 0.517Pl(Ab_{97}) + 0.191\ Kfs(Or_{98}) + 0.172\ Ill + 0.125\ Cal + 0.197\ H_2O + 1.383\ H^+ + 0.084\ Ca^{2+} + 0.236\ Na^+$ (Table 5)

The conservations (2), (3), (4) and (5) give:

$Pl(Ab_{74}) + 0.321\ H_4SiO_4 + 0.120\ CO_2 + 0.384\ Al^{3+} + 0.015\ Fe^{2+} + 0.013\ Mg^{2+} + 0.370\ K^+ + 0.007\ F^- \rightarrow 0.498\ Pl(Ab_{97}) + 0.184\ Kfs(Or_{98}) + 0.166\ Ill + 0.120\ Cal + 0.070\ H_2O + 1.146\ H^+ + 0.090\ Ca^{2+} + 0.256\ Na^+$ (Table 5)

Both reactions represent the albitization, K-feldspathization, and production of illite and calcite by the consumption of plagioclase with an inflow of H_4SiO_4, CO_2, Al^{3+}, Fe^{2+}, Mg^{2+}, K^+, and F^- from the hydrothermal fluid, accompanied by the outflow of H_2O, H^+, Ca^{2+}, and Na^+ into the hydrothermal fluid (Fig. S6A). Two overall reactions have a difference in the amounts of inflow components. The amounts of inflow components in the later reaction (volume reduction) is smaller than that of the former reaction (constant volume alteration), accompanying that the later reaction occurs a smaller amounts of mineral products and a

larger amounts of outflow components (Ca^{2+} and Na^{+}) relative to the former reaction. The plagioclase alteration reactions for Types A-2, A-3, B-1, B-2, C-1, C-2, C-3-1, C-3-2, and C-3-3 are described in Appendix B. Figure S6 shows the characteristics of these reactions and gives their inflow and outflow components through the hydrothermal fluid.

Characteristics of mass transfer leading to plagioclase alteration. Plagioclase alteration involving albitization and the formation of associated minerals is characterized by the following significant features: an inflow of H_4SiO_4, Al^{3+}, Fe^{2+}, Mn^{2+}, Mg^{2+}, K^{+}, CO_2, and F^{-} and an outflow of H_2O, H^{+}, and Ca^{2+} (Table 5; Fig. S6). Albitization is characterized by that the consumption of plagioclase with an inflow of H_4SiO_4 and Na^{+} and an outflow of Al^{3+} and Ca^{2+} into the hydrothermal fluid (e.g. Type A-3). We confirmed both the inflow and outflow of Na^{+} in the overall reactions (Table 5). The inflow of sodium ions produces a large volume of albite (Fig. S6B, C, F, and J). In the absence of sodium ion inflow, some of the Na^{+} dissolved from plagioclase due to the formation of micropores is used in albitization, while the rest is released into the hydrothermal fluid (Fig. S6A, D, E, G, and H). Both the inflow and outflow of aluminum ions are closely related to the formation of illite. The inflow of aluminum ions produces a large volume of illite (more than 10% volume) within an alteration area (Fig. S6A, B, D, E, F, H, and J): e.g., the alteration area in the Type A-1 sample contained an illite volume of about 23% (Table 2). In case of absence of an Al^{3+} inflow, some of the aluminum ions dissolved from plagioclase due to the formation of micropores yield a small volume of illitization (e.g., 4 vol% for an alteration area in Type C-3-2: Table 2), while the rest are released into the hydrothermal fluid (Fig. S6C, F and I).

Petrographical observations shows that altered plagioclase with more than 10 vol% illite in the alteration area occurs with high frequency in the samples (Fig. 4; Table 2). Thus, the inflow of aluminum ions is a dominant characteristic in the mass transfer of plagioclase alteration. The inflow of Fe^{2+}, Mn^{2+}, and Mg^{2+} from the hydrothermal fluid into the plagioclase results in the production of illite (Fig. S6A, B, D, E, F, H, I, and J). Hydrogen ions are frequently observed as a product (right-hand side) in the overall reactions (e.g., the Type A-1 and A-2 reactions of Table 5). Therefore, there is a gradual increase in the H^+ concentration of the hydrothermal fluid as the plagioclase alteration proceeds, indicating a gradual decrease in pH in the hydrothermal fluid. The alteration reactions for type A-3 indicate the production of a small amount of K-feldspar at chemical compositions below Or_{90} (Table 1 and 2), and the release of K^+ into the hydrothermal fluid (Table 5). The mass transfer of chlorine is not included in the Type A-1, B-1, and C-2 reaction equations even though chlorine-bearing illites are a product because the illites contain less than 0.001 chlorine atoms per formula unit (apfu) (Table 5).

Thermal and temporal relationships between plagioclase alteration and biotite chloritization

By determining the temporal and thermal conditions and the chemical characteristics of biotite chloritization and plagioclase alteration, the temporal sequence of the fluid chemistry in the pluton over a wide temperature range during sub-solidus cooling can be interpreted.

Determination of the thermal conditions during the plagioclase alteration. The illite

This is a preprint, the final version is subject to change, of the American Mineralogist (MSA)
Cite as Authors (Year) Title. American Mineralogist, in press.
DOI: https://doi.org/10.2138/am-2019-6786

K-Ar dating of sample No. 06MI03-8 gives an age of 59.2 ± 1.4 Ma (Table 3). The thermal condition of illite was determined from its age using the *t-T* path of sample DH2 RA03 (-302.1 masl of borehole DH2) within the Toki granite (Fig. 10A). Sample DH2 RA03 was obtained from a location close to the sample location of this study (about 90 m away in horizontal distance: Fig. 1D). The *t-T* path of sample DH2 RA03 was constructed from the thermochronological data, including the ages of zircon U-Pb, biotite K-Ar, ZFT, and AFT and the FT inverse calculation (Yuguchi et al. 2018). The FT inverse calculation was derived from the data set including the AFT age, AFT lengths, ZFT age, and ZFT lengths, and provided the acceptable-fit paths, good-fit paths, best fit path, and weighted mean path below 400 °C; the FT inverse calculation was described in detail by Yuguchi et al. (2018). The envelope of good-fit paths include the biotite K-Ar, ZFT, and AFT ages, resulting in the reasonable reproduction of the *t-T* path from the biotite K-Ar closure temperature (350–400 °C) through the ZFT partial annealing zone (PAZ) (190–390 °C) to the AFT PAZ (60–120 °C). Therefore, the weighted mean *t-T* path was employed for this discussion. The intersection of the *t-T* path and the age of 59.2 ± 1.4 Ma (blue lateral lines) gives a range of 290 to 305 °C for the formation temperature (Fig. 10B). The closure temperature of the illite K-Ar geochronometry has never been determined unambiguously because it strongly depends on the grain size (Dodson 1973; Harrison et al. 2009). Previous experimental and empirical data suggests a closure temperature lower than 300 °C for a clay-size illite (Garduño-Martínez et al. 2015). This closure temperature is consistent with the thermal condition at which the *t-T* path intersects with the age of 59.2 ± 1.4 Ma.

Determination of the temporal conditions of biotite chloritization. Yuguchi et al. (2015) revealed the temperature conditions at which biotite chloritization occurred based on chlorite geothermometers. This study employed the same samples as Yuguchi et al. (2015). The chloritization temperature conditions were found to range from 180 to 350 °C (Yuguchi et al. 2015), but the formation age could not be determined due to the absence of geochronometry applicable to chlorite. The age of the chlorite was determined from the temperature condition using the *t*-*T* path of sample DH2 RA03. The intersection of the weighted mean *t*-*T* path and the thermal condition of 350 °C (blue horizontal line) give a formation age of about 68 Ma, and that of the *t*-*T* path and the thermal condition of 180 °C give an age of about 51 Ma (Fig. 10C), which indicates that biotite chloritization occurred over a period of about 17 million years from about 68 to 51 Ma.

The temporal and thermal relationships between biotite chloritization and plagioclase alteration. Having determined both the temporal and thermal conditions for biotite chloritization and plagioclase alteration, we could then discuss the sequential relationship between these processes. The temporal and thermal conditions of biotite chloritization (68–51 Ma and 350–180 °C) overlapped with that of plagioclase alteration (59.2 ± 1.4 Ma and 290–305 °C). The temporal and thermal consistency between the two processes indicates that the serial alteration processes from biotite chloritization to plagioclase alteration occurred during 68–51 Ma and at a temperature condition of 350–180 °C within the rock body.

This is a preprint, the final version is subject to change, of the American Mineralogist (MSA)
Cite as Authors (Year) Title. American Mineralogist, in press.
DOI: https://doi.org/10.2138/am-2019-6786

Sequential variations in the chemical characteristics of the hydrothermal fluid.

The overall reactions for Types A–C plagioclase alteration (Table 5) give the exchange of components between the plagioclase and hydrothermal fluid during alteration: the inflow of components from the hydrothermal fluid to the plagioclase and the outflow of components from the plagioclase to the hydrothermal fluid. The alteration reactions are characterized by the following significant features: reaction with the inflow of H_4SiO_4, Al^{3+}, Fe^{2+}, Mn^{2+}, Mg^{2+}, K^+, CO_2, and F^- and the outflow of H_2O, H^+, and Ca^{2+} (Fig. S6). The inflow components of plagioclase alteration H_4SiO_4 (Si^{4+}), K^+, and F^- correspond to the outflow components of biotite chloritization (Fig. 11). Biotite chloritization is the dominant source of mass transfer to produce the plagioclase alteration because of the consistency between the outflow components of biotite chloritization and the inflow components of plagioclase alteration and the connection of the micropores from chlorite to the plagioclase alteration area. That is, there is a sequence of mass transfer from biotite chloritization to plagioclase alteration in the hydrothermal alteration. Both chloritization and plagioclase alteration occur ubiquitously in the Toki granitic rock body, which impacts the fluid chemistry through the hydrothermal convection throughout the pluton; the ongoing reactions decrease the concentration of the inflow components and increase the concentration of outflow components in the hydrothermal fluid. The reactions of biotite chloritization and plagioclase alteration represent the sequential variations in the fluid chemistry at the temporal conditions from 68 Ma to 51 Ma as the temperature cooled from 350 to 180 °C (Fig. 11).

Although the outflow of H_4SiO_4 (Si^{4+}) and K^+ during chloritization cause a short-term increase in the concentrations of these components in the hydrothermal fluid, the inflow of

H_4SiO_4 (Si^{4+}) and K^+ to the plagioclase alteration process can prevent or cancel out this increase. As a result, there is no significant increase or decrease in the concentration of H_4SiO_4 (Si^{4+}) and K^+ in the fluid after the two hydrothermal alteration events. Chloritization releases fluorine ions from biotite (Yuguchi et al. 2015). Small amounts of these fluorine ions are used in the plagioclase alteration reactions (Table 5) and trapped in illite. However, because illite contains only a small amount of fluorine, less than 0.04 wt% (Table 1 and S1), the majority of the fluorine ions are released in the hydrothermal fluid. Therefore, the concentration of fluorine ions in the fluid gradually increases as the alteration proceeds (Fig. 11). Chloritization and plagioclase alteration require the consumption of aluminum, iron (ferrous), manganese, and magnesium ions (Fig. 11). Therefore, the concentrations of aluminum, iron, manganese, and magnesium ions in the fluid decrease gradually as the chloritization and plagioclase alteration proceed (Fig. 11). The plagioclase alteration is accompanied by the outflow of calcium ions, and thus their concentration in the hydrothermal fluid gradually increases as the alteration proceeds (Fig. 11). The calcium ions released from plagioclase precipitate as carbonate minerals after the two hydrothermal alteration events (Nishimoto et al. 2008).

The biotite chloritization and plagioclase alteration reactions also reveal temporal variations in the potential of hydrogen (pH) of the hydrothermal fluid. The hydrogen ion is a component of the outflow of the plagioclase alteration reactions (Fig. 11). Thus, a gradual increase of in the concentration of H^+, i.e., a gradual decrease of the pH of the fluid, occurs as the plagioclase alteration proceeds. On the other hand, the pH of the fluid gradual increases as the chloritization proceeds (Yuguchi et al. 2015). The changes in the

physicochemical parameters of the fluid due to chloritization influenced and advanced the subsequent plagioclase alteration because hydrothermal fluid with a high pH enhances the dissolution of plagioclase (Yasuhara et al. 2012). The dissolution of plagioclase led to the formation of micropores, which corresponds to the incipient stage of plagioclase alteration. As the plagioclase alteration proceeded, the pH of the hydrothermal fluid decreased, resulting in the stoppage of plagioclase dissolution (Fig. 11).

Mass transfer rate and the reaction rim in the plagioclase alteration.

Mass transfer rate through micropores within plagioclase. The factors contributing to plagioclase alteration are the distribution and the direction of the extension of the micropores, and the mass transfer of the components released by biotite chloritization. We estimated the mass transfer rate through the micropores, which resulted in the plagioclase alteration.

The Type A-2 sample (No. 9-8) shows overall alteration due to contact with chlorite, and the Type C-1 (No. 6-6), C-3-1 (No. 7-6), and C-3-3 (No. 9-9) samples show rim alteration due to contact with chlorite (Fig. 12 and S7). In each sample, the long axis direction of micropores is consistent with the direction of associated minerals, extending towards the chlorite (Fig. 12A and B). The determination of mass transfer rate has some uncertainty in case that the spatial relation between altered plagioclase and chloritized biotite is not constrained. The four cases allow us to evaluate the rate of mass transfer inward through the micropores within the plagioclase from the margin in contact with chlorite on the assumption that mass transfer occurred parallel to the observation plane. We define the maximum hydrothermal fluid infiltration (HFI) rate as the maximum distance from the

This is a preprint, the final version is subject to change, of the American Mineralogist (MSA)
Cite as Authors (Year) Title. American Mineralogist, in press.
DOI: https://doi.org/10.2138/am-2019-6786

margin to the alteration (albite) front (e.g., 750 μm in the Type A-2 sample: Fig. 12A) divided by the alteration duration. To determine the HFI rate, we estimated the alteration duration as follows. The temperature determined from the composition of the rim chlorite corresponds to the thermal condition under which the biotite chloritization started (Yuguchi et al. 2015). This thermal condition is interpreted as the onset temperature of plagioclase alteration because the chloritization and plagioclase alteration occurred serially. In the Type A-2 sample, the onset temperature of plagioclase alteration determined by the rim composition of the chlorite in contact with the altered plagioclase was about 340 °C, based on analysis No. 116 (Fig. 12A). The intersection of the weighted mean *t*-*T* path of the sample DH2 RA03 and the thermal condition of 340 °C give an onset age of about 66 Ma for the plagioclase alteration (Fig. 12C). The combination of albite and K-feldspar close to the alteration front can give the terminal temperature of alteration through ternary feldspar thermometry; e.g., the compositions of analyses No. J22 and J25 in the Type C-3-1 sample give a temperature of about 280 °C using the ternary feldspar thermometer of Furman and Lindsley (1988) (Table 1 and Fig. S2C-7). At such low temperatures, an exact estimation of temperature is not possible due to ordering and kinetic effects. Yuguchi et al. (2015) suggested thermal conditions ranging from about 180 to 350 °C for biotite chloritization. In this study, the terminal temperature of chloritization, about 180 °C, is defined as the terminal temperature of plagioclase alteration. In the Type A-2 sample, the intersection of the weighted mean *t*-*T* path and thermal condition of 180 °C gives a termination age of about 51 Ma (Fig. 12C), which indicates that the plagioclase alteration occurred over a period of about 15 million years, from about 66 to 51 Ma. Thus, the maximum HFI rate of the Type A-2

plagioclase can be calculated to be about 50.0×10^{-6} μm/year (750 μm/15 m.y.). The same analyses were employed for the Type C-1, C-3-1, and C-3-3 samples (Fig. S7A, B and C). The maximum HFI rates for these four samples range from 38.0×10^{-6} to 68.1×10^{-6} μm/year.

The maximum distance from the margin to the K-feldspar (or illite) front (e.g., 738 μm in the Type A-2 sample: Fig. 12A) is smaller than the maximum distance from the margin to the alteration front. Here we define the maximum rate of potassium transfer (KT rate) as the maximum distance from the margin to the K-feldspar (or illite) front divided by the alteration duration because the potassium ions for the formation of K-feldspar (or illite) during plagioclase alteration are supplied predominantly from the biotite chloritization. The maximum KT rate in the Type A-2 plagioclase is estimated to be about 49.2×10^{-6} μm/year (738 μm/15 m.y.). The same analyses were employed for the Type C-1, C-3-1, and C-3-3 samples (Fig. S7A, B and C). The maximum KT rates for the four samples range from 36.3×10^{-6} to 64.1×10^{-6} μm/year, which are slightly smaller than the maximum HFI rates.

Reaction rate of the plagioclase alteration. Wood and Walther (1983) and Walther and Wood (1984) discussed the rates of hydrothermal reactions and prograde metamorphic reactions, respectively. They presented a method to calculate the reaction rate in units of gram atom oxygen cm^{-2} s^{-1}. We estimated the reaction rate of the plagioclase alteration for the Type A-2 (No. 9-8), C-1 (No. 6-6), C-3-1 (No. 7-6) and C-3-3 (No. 9-9) samples according to their method. The plagioclase alteration is accompanied essentially with albitization, which requires the addition of silicon ions (Table 5 and Fig. S6). The inflow

of silicon ions is supplied by biotite chloritization (Fig. 11). Therefore, we utilized the molar variation of silicon dioxide between the reactant (the original plagioclase) to the product (albite) as the number of moles supplied (Molar variation of Table 6) to determine the reaction rate. The calculation of reaction rate requires the following parameters (Walther and Wood 1984): the radius of the circle (Radius of Table 6), assuming the albite area to be circular, the distance from chlorite to the HFI front per unit area (Distance of Table 6), the solubility of quartz at the alteration conditions (Solubility of Table 6), and the alteration duration (Duration of Table 6). The distance and duration were provided in the above discussion. The albite area was obtained from the alteration area (Table 4) and the volume ratios of the product minerals (Table 2). Assuming alteration conditions of 100–500 MPa and 200–400 °C, the solubility of quartz was defined as 10^{-4} mol cm^{-3} (Walther and Helgeson 1977). The calculated reaction rates for the Type A-2, C-1, C-3-1, and C-3-3 samples range from 9.25×10^{-13} to 3.45×10^{-12} gram atom oxygen cm^{-2} s^{-1} (Table 6). These values are very consistent with the reaction rates compiled by Wood and Walther (1983) under wide temperature conditions, which were determined from dissolution experiments and phase equilibrium studies. There is a strong correlation between the reaction rate and temperature given by $\log k \simeq -2900/T - 6.85$, where k stands for the reaction rate (gram atom oxygen cm^{-2} s^{-1}) and T is the temperature. The plagioclase alteration of the Types A-2, C-1, C-3-1, and C-3-3 samples occurred at temperature conditions of 180–340 °C (Fig. 12 and S7). These temperature conditions enable us to calculate the approximate reaction rate through the correlation of Wood and Walther (1983), giving reaction rates ranging from 5.60×10^{-14} to 2.63×10^{-12} gram atom oxygen cm^{-2} s^{-1}. The mass transfer rate and reaction rate

This is a preprint, the final version is subject to change, of the American Mineralogist (MSA)
Cite as Authors (Year) Title. American Mineralogist, in press.
DOI: https://doi.org/10.2138/am-2019-6786

are possible indicators to relate the extent of hydrothermal alteration in plagioclase to the time scale.

This is a preprint, the final version is subject to change, of the American Mineralogist (MSA)
Cite as Authors (Year) Title. American Mineralogist, in press.
DOI: https://doi.org/10.2138/am-2019-6786

IMPLICATIONS

This paper presents a new interpretation of the role of micropores in plagioclase on hydrothermal alteration of granitic rocks, which has been overlooked or not fully appreciated in previous studies. Our work has been benefited from fresh samples taken from deep boreholes at the depth of 500 m from the surface, which enabled us to observe the micropores in plagioclase. Such micropores have not been observed easily in samples taken from the surface outcrops or from boreholes near surface due to weathering, indicating the importance of studying fresh samples to clarify the nature of hydrothermal alteration of granitic rocks.

This paper clarified that the micropores have a crucial role to the serial hydrothermal alteration processes from biotite chloritization to plagioclase alteration in a granitic pluton, by presenting a new methodology to evaluate the mass transfer through the micropores. The chemical characteristics of secondary minerals of hydrothermal origin contribute to reveal the sequential variations in the fluid chemistry. This paper further discussed that the position-specific *t*-*T* path is an effective tool for determining unknown thermal (or temporal) conditions from already-known temporal (or thermal) conditions of the target mineral. The mass transfer rate and reaction rate are possible indicators to relate the degree and extent of plagioclase alteration to the time scale, which were made possible by determinations of the alteration duration. This study dealing with role of micropores, mass transfer and reaction rate provides important procedures and parameters for future forecasting of the geochemical features of a granitic rock. Our interpretations and methodology are quite new in this filed, and their validity and usefulness should be evaluated in future studies.

ACKNOWLEDGEMENTS

Constructive reviews by two anonymous reviewers and Dr. T. Mueller (associated editor) were very helpful in revising the manuscript. The authors thank the researchers of the Mizunami Underground Research Laboratory and the Toki Research Institute of Isotope Geology and Geochronology, Japan Atomic Energy Agency, for their discussion and suggestions. We would like to thank Editage (www.editage.jp) for English language editing. This work was financially supported by a JSPS KAKENHI for Young Scientists [grant number 16H06138] to TY.

REFERENCES CITED

Boulvais, P., Ruffet, G., Cormichet, J., and Mermet, M. (2007) Cretaceous Albitization and dequartzification of Hercynian peraluminous granite in the Salvezines Massif (French Pyrénées). Lithos, 93, 89-106.

Cathelineau, M. (1988) Cation site occupancy in chlorites and illites as a function of temperature. Clay Minerals, 23, 471-485.

Dalrymple, G.B., and Lanphere, M.A. (1969) Potassium-Argon Dating; Principles Techniques, and Applications to Geochronology. W. H. Freeman and Co., San Francisco, pp. 258.

Dalrymple, G.B., Grove, M., Lovra, O.M., Harrison, T.M., Hulen, J.B., and Lanphere, M.A. (1999) Age and thermal history of the Geysers plutonic complex (felsite unit), Geyers geothermal field, California: a ^{40}Ar / ^{39}Ar and U-Pb study. Earth and Planetary Science Letters, 173, 285-298.

Dodson, M.H. (1973) Closure temperature in cooling geochronological and petrological systems. Contributions to Mineralogy and Petrology, 40, 259-274.

Dodson, H., and McClelland-Brown, E. (1985) Isotopic and paleomagnetic evidence for rates of cooling, uplift and erosion. In: Snelling J (ed) Geological Society of London Memories 10, Oxford, London, pp. 315-325.

Eliasson, T. (1993) Mineralogy, geochemistry and petrophysics of red coloured granite adhacent to fractures. Swedish Nuclear Fuel and Waste Management Co. (SKB). SKB-TR-93-06.

Ferry, J.M. (1979) Reaction mechanisms, physical conditions and mass transfer during hydrothermal alteration of mica feldspar in granitic rocks from South Central Maine, U.S.A. Contributions to Mineralogy and Petrology, 68, 125-139.

Fuhrman, M.L., and Lindsley, D.H. (1988) Ternary-feldspar modeling and thermometry. American Mineralogist, 73, 201-215.

Garduño-Martínez, D.E., Puig, T.P., Solé, J., Martini, M., and Alcalá-Martínez, J.R. (2015) K-Ar illite-mica age constraints on the formation and reactivation history if the E1 Doctor fault zone, central Mexico. Revista Mexicana de Ciencias Geológicas, 32, 306-322.

Grove, M., and Harrison, M. (1996) ^{40}Ar* diffusion in Fe-rich biotite. American Mineralogist, 81, 940-951.

Hey, M.H. (1954) A new review of the chlorites. Mineralogical Magazine, 30, 277-292.

Harrison, T.M., Celerier, J., Aikman, A.B., Hermann, J., and Heizler, M.T. (2009) Diffusion of ^{40}Ar in muscovite. Geochimica et Cosmochimica Acta, 73, 1039-1051.

Ishibashi, M., Ando, T., Sasao, E., Yuguchi, T., Nishimoto, S., and Yoshida, H. (2014) Characterization of water conducting fracture and their long-term behavior in deep crystalline rock: A case study of the Toki granite. Journal of the Japan Society of Engineering Geology, 55, 156-165 (in Japanese with English abstract).

Ishibashi, M., Yoshida, H., Sasao, E., and Yuguchi T. (2016) Long term behavior of hydrogeological structures associated with faulting: An example from the deep crystalline rock in the Mizunami URL, Central Japan. Engineering Geology, 208, 114-127.

Ishihara, S. (2003) Chemical contrast of the Late Cretaceous granitoids of the Sanyo and Ryoke Belts, Southwest Japan: Okayama-Kagawa Transect. Bulletin of the Geological

Survey of Japan 54, 95-116.

Ishihara, S., and Suzuki, Y. (1969) Basement granites of the Toki uranium deposits in Tono region. Reports of the Geological Survey of Japan, 232, 113-127.

Ishihara, S., and Chappell, B. (2007) Chemical compositions of the late Cretaceous Ryoke granitoids of the Chubu District, central Japan – Revisited. Bulletin of the Geological Survey of Japan, 58, 323-350.

Itaya, T., Nagao, K., Inoue, K., Honjou, Y., Okada, T., and Ogata, A. (1991) Argon isotope analysis by a newly developed mass spectrometric system for K-Ar dating. Mineralogical Journal, 15, 203-221.

Itoigawa, J. (1974) Geology of the Mizunami district, central Japan. Bulletin of the Mizunami Fossil Museum, 1, 9-42 (in Japanese).

Itoigawa, J. (1980) Geology of the Mizunami district, central Japan. Monograph of the Mizunami Fossil Museum, 1, 1-50 (in Japanese).

Japan Nuclear Cycle Development Institute (2000) Regional Hydrogeological Study Project Result from 1992-1999. JNC Technical Report, JNC TN7400 2003-007, Tono Geoscience Center.

Japan Nuclear Cycle Development Institute (2002) Master Plan of the Mizunami Underground Research Laboratory Project. JNC Technical Report. JNC TN7410 2003-001, Tono Geoscience Center.

Morad, S., El-Ghali, M.A.K., Caja, M.A., Sirat, M., Al-Ramadan, K., and Hansurberg, H. (2010) Hydrothermal alteration of plagioclase in granitic rocks from Proterozoic basement of SE Sweden. Geochemical Journal, 45, 105-116.

Nagao, K. Nishido, H., Itaya, T., and Ogata, K. (1984) An Age Determination by K-Ar Method. Bulletin of the Hiruzen Research Institute, Okayama University of Science, 9, 19-38 (in Japanese).

Nagao, K., and Itaya, T. (1988) K-Ar determination. Memoirs of the Geological Society of Japan, 39, 5-21.

Nishimoto, S., Ukai, E., Amano, K., and Yoshida, H. (2008) Alteration process in deep granitic rock - an example of Toki granite, central Japan. Journal of the Japan Society of Engineering Geology, 49, 94-104 (in Japanese with English abstract).

Nishimoto, S., and Yoshida, H. (2010) Hydrothermal alteration of deep fractured granite: Effects of dissolution and precipitation. Lithos, 115, 153-162.

Plümper, O., and Putnis, A. (2009) The Complex Hydrothermal History of Granitic Rocks: Multiple Feldspar Replacement Reactions under Subsolidus Conditions. Journal of Petrology, 50, 967-987.

Putnis, C.V., Austrheim, H., and Putnis, A. (2007) A mechanism of fluid transport through minerals. Geochimica et Cosmochimica Acta, 71, A814.

Sano, H., Yamagata, T., and Horibo, K. (1992) Tectonostratigraphy of Mino terrane: Jurassic accretionary complex of southwest Japan. Palaeogeography, Palaeoclimatology, Palaeoecology, 96, 41-57.

Shibata, K., and Ishihara, S. (1979) Rb-Sr whole-rock and K-Ar mineral ages of granitic rocks in Japan. Geochemical Journal, 13, 113-119.

Sonehara, T., and Harayama, S. (2007) Petrology of the Nohi Rhyolite and its related granitoids: a Late Cretaceous large silicic igneous field in central Japan. Journal of

Volcanology and Geothermal Research, 167, 57-80.

Steiger, R.H., and Jäger, E. (1977) Subcommission on geochronology: Convention on the use of decay constants in geo- and cosmochronology. Earth and Planetary Science Letters, 36, 359-362.

Suzuki, K., and Adachi, M. (1998) Denudation history of the high T/P Ryoke metamorphic belt, southwest Japan: constraints from CHIME monazite ages of gneisses and granitoids. Journal of Metamorphic Geology, 16, 27-37.

Todo Collaborative Research Group (1999) Fault bounded inland basin of multiple blocks: an example from the sedimentary basin of the Tokai Group around Tajimi City in Gifu Prefecture, central Japan. Earth Science, 53, 291-306.

Walther, J., and Helgeson, H.C. (1977) Calculation of the thermodynamic properties of aqueous silica and the solubility of quartz and its polymorphs at high pressure and temperature. American Journal of Science, 277, 1315-1351.

Walther, J., and Wood, B.J. (1984) Rate and mechanism in prograde metamorphism. Contributions to Mineralogy and Petrology, 88, 246-259.

Wood, B.J., and Walther, J. (1983) Rates of hydrothermal reactions. Science, 28, 413-415.

Yagi, K. (2006) Manual of mineral separation for K-Ar age dating. Engineering Geology of Japan, 0 ‘The special issue of 10th aniversary of Hiruzen Institute for Geology and Chronology’, 19-25 (in Japanese).

Yagi, K., and Itaya, T. (2011) Influence of K-Ar age on the major minerals by treatment with hydrochloric acid. Engineering Geology of Japan, no. 1, 37-43 (in Japanese).

Yagi, K., Okada, T., Honjou, Y., and Itaya, T. (2015) Argon analyses by isotopic dilution

method using argon 38 spike with HIRU -Reproducibility and reliability in 25 years K-Ar dating-. Bulletin of the Research Institute of Technology, Okayama University of Science, no. 33, 42-52.

Yamasaki, S., and Umeda, K. (2012) Cooling history of the Cretaceous Toki granite in the eastern Sanyo Belt, Central Japan. Japanese Magazine of Mineralogical and Petrological Sciences, 41, 39-46 (in Japanese with English abstract).

Yasuhara, H., Hashimoto, K., and Kinoshita, N. (2012) Evaluation of Dissolution Equation in Granite Examined by Flow-Through Dissolution Experiment under Temperature and pH Conditions Controlled. Journal of MMIJ, 128, 79-85.

Yoneda, T., and Maeda, H. (2008) The chemical composition of chlorites from hydrothermal ore deposits and its applicability to geothermometers. Journal of MMIJ, 124, 694-699.

Yuguchi, T., and Nishiyama, T. (2008) The mechanism of myrmekite formation deduced from steady-diffusion modeling based on petrography: Case study of the Okueyama granitic body, Kyushu, Japan. Lithos, 106, 237-260.

Yuguchi, T., Tsuruta, T., and Nishiyama, T. (2010) Zoning of rock facies and chemical composition in the Toki granitic body, Central Japan. Japanese Magazine of Mineralogical and Petrological Sciences, 39, 50-70 (in Japanese with English abstract).

Yuguchi, T., Tsuruta, T., and Nishiyama, T. (2011A) Three-dimensional cooling pattern of a granitic pluton I: The study of exsolution sub-solidus reactions in the Toki granite, Central Japan. Journal of Mineralogical and Petrological Sciences, 106, 61-78.

Yuguchi, T., Tsuruta, T., and Nishiyama, T. (2011B) Three-dimensional cooling pattern of a granitic pluton II: The study of deuteric sub-solidus reactions in the Toki granite, Central

Japan. Journal of Mineralogical and Petrological Sciences, 106, 130-141.

Yuguchi, T., Amano, K., Tsuruta, T., Danhara, T., and Nishiyama, T. (2011C) Thermochronology and the three-dimensional cooling pattern of a granitic pluton: An example of the Toki granite, Central Japan. Contributions to Mineralogy and Petrology, 162, 1063-1077.

Yuguchi, T., Tsuruta, T., Hama, K., and Nishiyama, T. (2013) The spatial variation of initial ^{87}Sr / ^{86}Sr ratios in the Toki granite, Central Japan: Implications for the intrusion and cooling processes of a granitic pluton. Journal of Mineralogical and Petrological Sciences, 108, 1-12.

Yuguchi, T., Sasao, E., Ishibashi, M., and Nishiyama, T., (2015) Hydrothermal chloritization process from biotite in the Toki granite, Central Japan: Temporal variation of chemical characteristics in hydrothermal fluid associated with the chloritization. American Mineralogist, 100, 1134-1152.

Yuguchi, T., Iwano, H., Kato, T., Sakata, S., Hattori, K., Hirata, T., Sueoka, S., Danhara, T., Ishibashi, M., Sasao, E., and Nishiyama, T. (2016) Zircon growth in a granitic pluton with specific mechanisms, crystallization temperatures and U-Pb ages: Implication to the 'spatiotemporal' formation process of the Toki granite, central Japan. Journal of Mineralogical and Petrological Sciences, 111, 9-34.

Yuguchi, T., Sueoka, S., Iwano, H., Danhara, T., Ishibashi, M., Sasao, E., and Nishiyama, T. (2017) Spatial distribution of the apatite fission-track ages in the Toki granite, central Japan: Exhumation rate of a Cretaceous pluton emplaced in the East Asian continental margin. Island Arc, 26, e12219 (1-15).

Yuguchi, T., Sueoka, S., Iwano, H., Izumino, Y., Ishibashi, M., Danhara, T., Sasao, E. Hirata, T., and Nishiyama, T. (2018) Region-by-region cooling paths within the Toki granite, central Japan: their constrained factors and the relation with fracture population in a pluton. Journal of Asian Earth Sciences, in press.

This is a preprint, the final version is subject to change, of the American Mineralogist (MSA)
Cite as Authors (Year) Title. American Mineralogist, in press.
DOI: https://doi.org/10.2138/am-2019-6786

Figure captions

Figure 1. The Toki granitic pluton and the Mizunami Underground Research Laboratory. (A) Map of Southwest Japan showing the location of the Toki granite (Tono district - TKG; square symbol) in central Japan, together with the distribution of the San-in, Sanyo and, Ryoke Belts in the Inner Zone of Southwest Japan, after Ishihara and Chappell (2007). (B) Geologic map of the Toki granite after Itoigawa (1980), the Mizunami Underground Research Laboratory and the borehole sites. The topographic contours inside the Tono district are based on Geographical Survey Institute 1:25,000 topographic maps entitled Mitake, Takenami, Toki, and Mizunami. Borehole investigations at the Toki granite were performed by the Japan Atomic Energy Agency for the 'Regional Hydrological Study (Japan Nuclear Cycle Development Institute 2000)' and the 'Mizunami Underground Research Laboratory Project (Japan Nuclear Cycle Development Institute 2002)'. (C) Rock facies cross-section of the Toki granite along the line from X to X' on the geologic map (Fig. 1B). MBG: muscovite-biotite granite, HBG: hornblende-biotite granite, and BG: biotite granite (Yuguchi et al. 2010). (D) Location of the shafts and boreholes in the Mizunami Underground Research Laboratory. (E) Schematic overview of the shafts, access/research galleries, sub-stages, and measurement niches of the Mizunami Underground Research Laboratory and the sample locations used in this study. The samples were collected from the borehole 06MI03 at altitudes ranging from -274 masl (meters above sea level) to -314 masl in the HBG of the Toki granite.

Figure 2. Polarization microscope (under crossed polars) images of unaltered (A) and altered (B, C and D) plagioclases. (A) Plagioclase without alteration (sample No. 6-10). (B) Overall alteration throughout the entire plagioclase grain (Type A), with varying volume ratios of associated minerals: high ratio (samples No. 8-7 and No. 9-8: B-1 and B-2) and low ratio (No. 12-7: B-3) samples. (C) Core alteration (Type B) with a restricted distribution (sample No. 12-2: C-1) and with wide distribution at not only the cores but also the rims (No. 7-8: C-2). (D) Rim alteration (Type C); partial distribution at the rims (sample No. 6-6: D-1, No. 6-9: D-2, and No. 7-6: D-3) and wide distribution (No. 9-4: D-4 and No. 9-9: D-5).

Figure 3. Frequency distributions of minerals in unaltered plagioclase and Type A, B, and C samples.

Figure 4. Backscattered electron (BSE) images of unaltered plagioclase (A) and the Type A (B), Type B (C), and Type C (D) plagioclase.

Figure 5. Chemical compositions of feldspar, illite, and chlorite. (A) Compositional plots of the intact unaltered plagioclase and albite and K-feldspar in the alteration area. (B) Compositional plots of the Fe/(Fe+Mg) ratio to Si for illite. (C) Compositional plots of chlorite on the classification diagram of Hey (1954), corresponding to ripidolite.

Figure 6. BSE images showing the irregular boundary of alteration front of Type C (A), the channel structure of hydrothermal fluid infiltration (HFI) (B), the mottled distribution of alteration area (C) the distribution of the micropores in the alteration area (D and E), and the relationship between the alteration area and sub-solidus reaction texture (F). (A) Type C (sample No. 9-9) shows irregular (uneven) alteration front in contact with intact area. (B) Sample No. 9-4 shows the channel structure of HFI and the differences between the distribution of micropores in the alteration area and intact area. (C) The alteration area shows a mottled distribution. (D and E) The differences in the distribution of micropores among albite, K-feldspar, illite, and calcite within the alteration area of sample No. 12-2. The micropores (and channels) are innate characteristics of the observed minerals, that is, they were not produced by partial losses of minerals in the processes of cutting and polishing. If the partial losses of minerals are produced in the processes of cutting and polishing, the clay minerals such as illite should contain large amounts of micropores. Within the altered area, however, albite and K-feldspar contained more micropores than illite, calcite, and fluorite. (F) Although the alteration area contained a large amount of micropores, the sub-solidus reaction rim does not contain micropores (sample No. 12-2).

Figure 7. Image analysis revealing the area (μm^2) and volume fraction of the micropores in the alteration area as determined by image processing software using samples No. 12-2 (A) and 9-4 (B) as examples. The alteration area containing the micropores was clipped from the BSE image (A-1) using the image processing software Photoshop®. The

micropores (and microcracks) were extracted from the alteration area through binary image processing using the Scion image program and counting the black pixels of A-2 (92,958 pixels). The pixel counts of the micropores were divided by the total pixel count of the alteration area (1,568,602 pixels: A-3) to give the volume (areal) fraction of the micropores (0.059). Image analysis of Sample No. 9-4 (B-1) gave the volume fractions of the micropores in the alteration area (0.067: B-2) and the intact area (0.023: B-3).

Figure 8. Dispersion diagram between the micropore area and the alteration, i.e., the HFI area, of the plagioclase, giving a good correlation ($R^2 = 0.9957$).

Figure 9. Direction of the associated minerals and the long axis direction of micropores in the alteration area of samples No. 9-9. Arrows indicate the direction of mass transfer from the chlorite into the plagioclase.

Figure 10. The *t-T* path determining both the temporal and thermal conditions of the secondary minerals. (A) The *t-T* path of sample DH2 RA03 is constructed from thermochronological data including zircon U-Pb ages, biotite K-Ar age, ZFT age, AFT age, and the FT inverse calculation. (B) Illitization during plagioclase alteration, for which the temporal condition is already known by K-Ar chronology, has an unknown thermal condition. The intersection of the weighted mean *t-T* path and the temporal condition of 59.2 ± 1.4 Ma (blue lateral lines) gives a thermal range from about 305 °C to 290 °C for the illitization. (C) The temporal condition for biotite chloritization, for which the

thermal condition is already known (Yuguchi et al. 2015), is obtained through the weighted mean *t*-*T* path. The intersection of the weighted mean *t*-*T* path and the thermal condition of 350 °C (blue horizontal line) gives a formation age of about 68 Ma, and that of the *t*-*T* path and a thermal condition of 180 °C gives an age of about 51 Ma, which indicates that the biotite chloritization occurred over about 17 million years, from about 68 to about 51 Ma.

Figure 11. Schematic figure showing the mass transfer of chemical components through the hydrothermal fluids in biotite chloritization and plagioclase alteration.

Figure 12. Mass transfer rate, including the hydrothermal fluid infiltration rate (HFI rate) and potassium transfer rate (KT rate), through the micropores within plagioclase using samples No. 9-8 (Type A) as examples. The HFI distance is defined as the distance from the chlorite margin to the alteration front, and the K-feldspar (illite) front distance is defined as the distance from the chlorite margin to the K-feldspar (illite) front (A). The direction of hydrothermal fluid infiltration and mass transfer are deduced from the long axis direction of micropores in the HFI area and the position of the chlorite in contact with the target plagioclase (B). The chloritization onset temperature was determined from the chemical composition of the chlorite margin (analysis No. 116) through the chlorite thermometer, giving a temperature condition of about 340 °C. The terminal temperature of chloritization, which was taken from Yuguchi et al. (2015), is about 180 °C. The intersection of the weighted mean *t*-*T* path and thermal condition of 340 °C gives about 66

Ma as the start age and that of the *t*-*T* path and thermal condition of 180 °C gives about 51 Ma, indicating that the biotite chloritization occurred over about 15 million years (C). The chloritization duration indicates the period over which mass transfer from the chlorite into the plagioclase continued to occur, and thus it can be defined as the duration of plagioclase alteration. The HFI distance divided by the plagioclase alteration duration gives the HFI rate of 50.0×10^{-6} μm/year, and the K-feldspar (illite) front length divided by the plagioclase alteration duration gives the KT rate of 49.2×10^{-6} μm/m.y.

Figure S1. BSE images (A-1 and B-1) and chemical maps showing the elemental Si, Al, Ca, Na, and K concentrations (A-2 to A-6 and B-2 to B-6) of samples No. 8-7 and No. 12-2. High concentrations are indicated by warm colors and low concentrations by cold colors. Illite, calcite, albite, and K-feldspar can be identified by the high concentrations of elemental Al, Ca, Na, and K, respectively.

Figure S2. BSE images of the altered Types A, B, and C plagioclases and the analysis points used to obtain their chemical compositions. The numbers correspond to the analysis points listed in Table 1 and S1.

Figure S3. XRD pattern of the 0.2–2.0 μm and >2.0 μm powder samples separated from the plagioclase of sample No. 06MI03-8, crystallographically confirming the occurrence of illite.

Figure S4. Direction of the associated minerals and the long axis direction of micropores in the alteration area of samples No. 7-6 (A) and 9-4 (B). Arrows indicate the direction of mass transfer from the chlorite into the plagioclase.

Figure S5. Image analysis revealing the volume (areal) ratios of the alteration minerals obtained using image processing software, with sample No. 9-8 as an example. (A) The alteration area containing the micropores was clipped from the BSE image using the image processing software Photoshop®. (B) The binary image processing using the Scion image software divided the image into black pixels, which includes the alteration area and chlorite (351,320 pixels), and white pixels, which corresponded to the unaltered area, micropores, microcracks, and areas other than the target alteration area (877,480 pixels). (C) Chlorite (3,412 pixels), giving an alteration area of 347,908 (351,320 – 3,412) pixels. (D) Sum of chlorite and fluorite (9,595 pixels), giving a fluorite count of 6,183 (9,595 – 3,412) pixels. (E) Sum of chlorite, fluorite, and calcite (13,881 pixels), giving a calcite pixel count of 4,286 (13,881 – 9,595) pixels. (F) Sum of chlorite, fluorite, calcite, and illite (67,104 pixels), giving an illite count of 53,223 (67,104 – 13,881) pixels. The pixel count of albite was determined subtracting chlorite, fluorite, calcite, and illite (67,104 pixels) the alteration area (347,908 pixels), giving an albite count of 280,804 pixels for sample No. 9-8.

Figure S6. Schematic figure showing the inflow and outflow of chemical components through the hydrothermal fluid during the plagioclase alteration.

This is a preprint, the final version is subject to change, of the American Mineralogist (MSA)
Cite as Authors (Year) Title. American Mineralogist, in press.
DOI: https://doi.org/10.2138/am-2019-6786

Figure S7. Mass transfer rate, including the hydrothermal fluid infiltration rate (HFI rate) and potassium transfer rate (KT rate), through the micropores within plagioclase using samples No. 6-6 (Type C: A), 7-6 (Type C: B), and 9-9 (Type C: C) as examples.

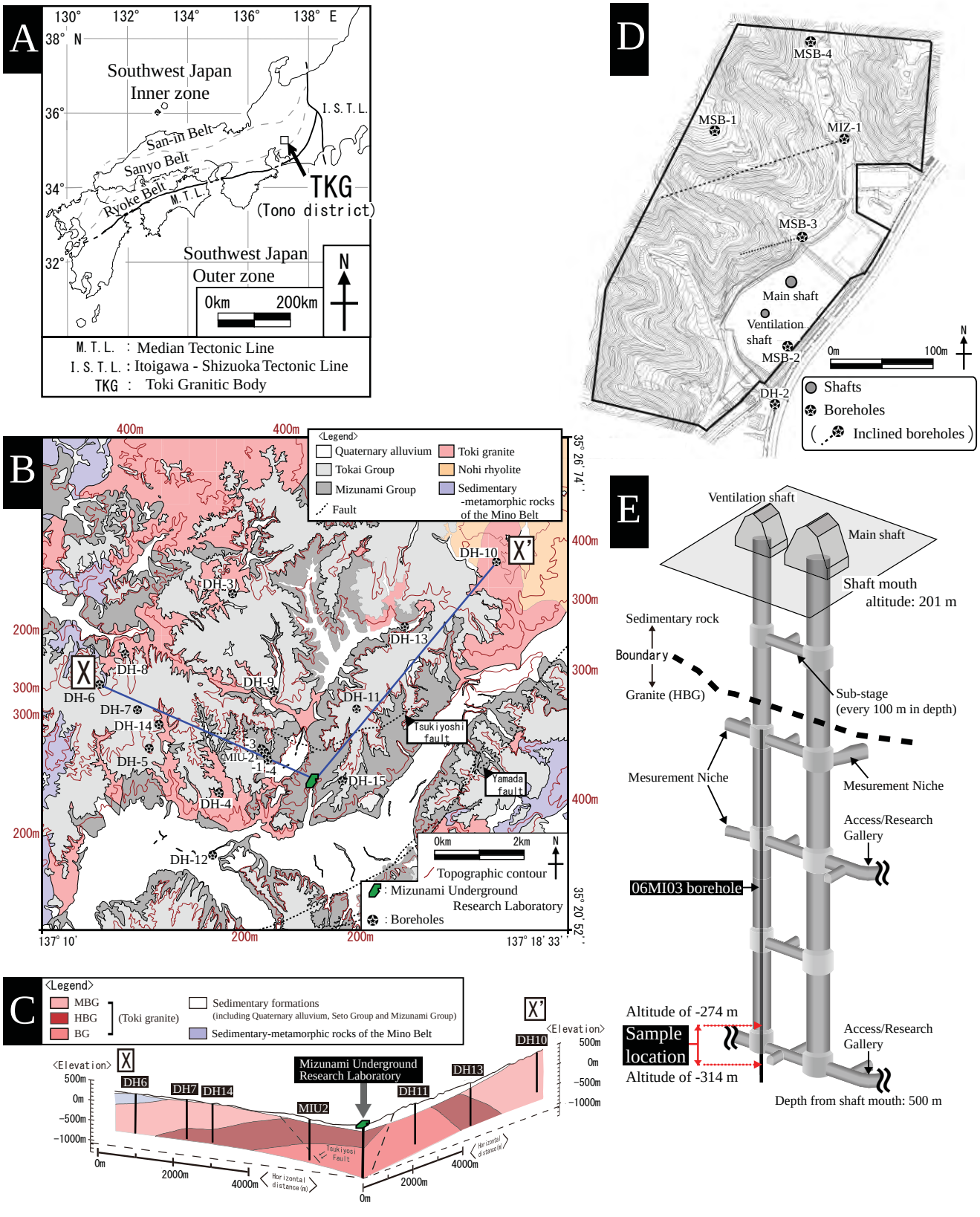

Yuguchi et al. Fig. 1

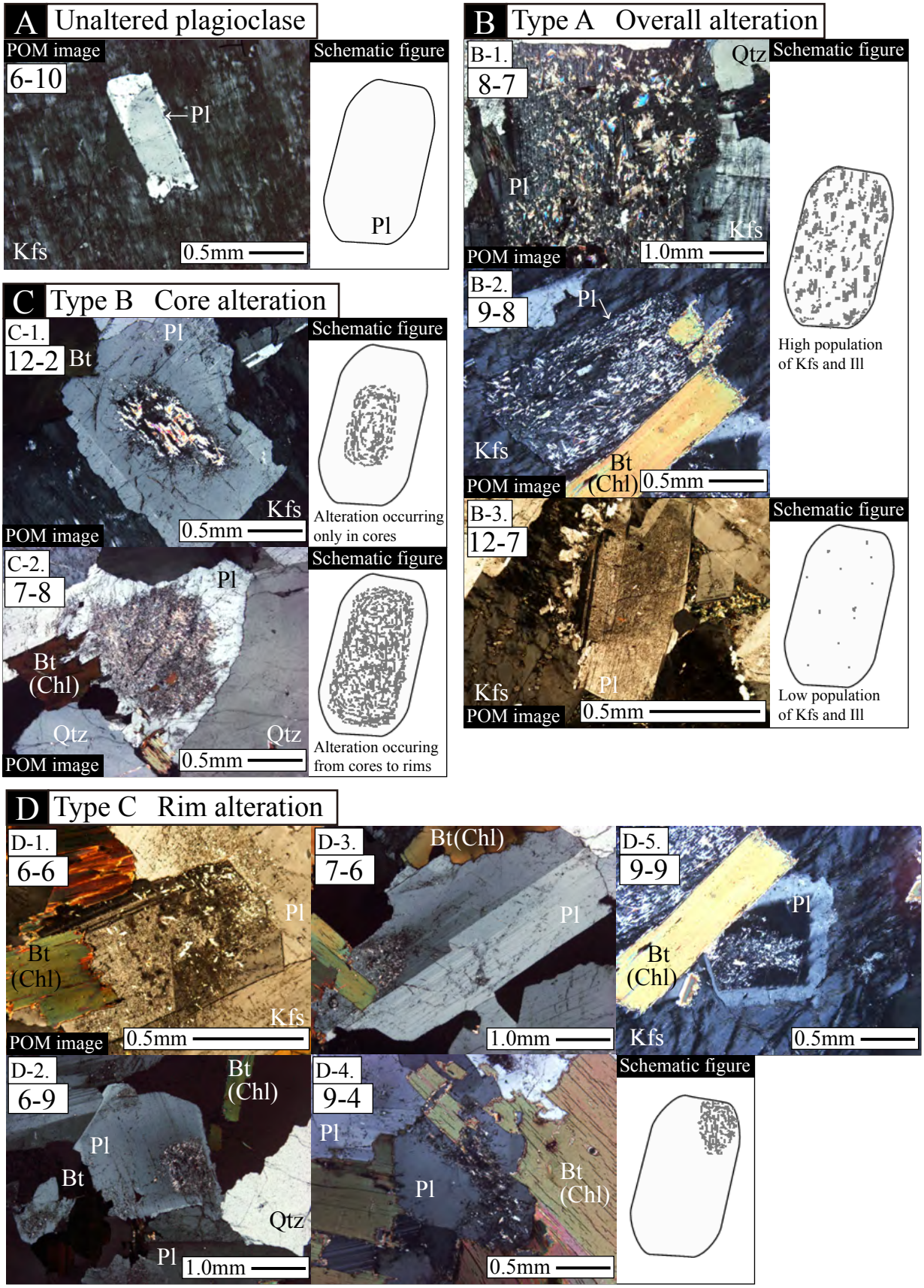

Yuguchi et al. Fig. 2

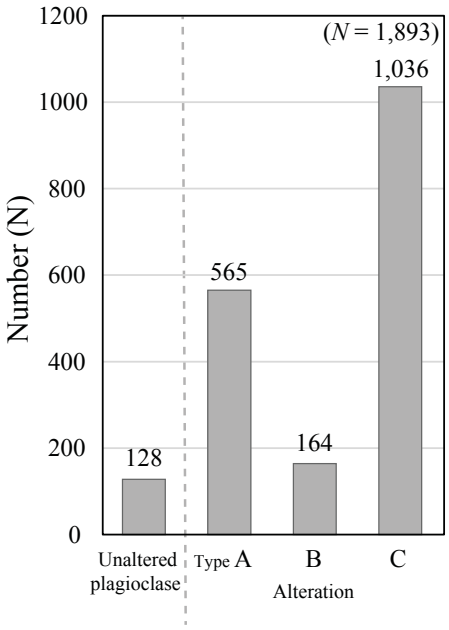

Yuguchi et al. Fig. 3

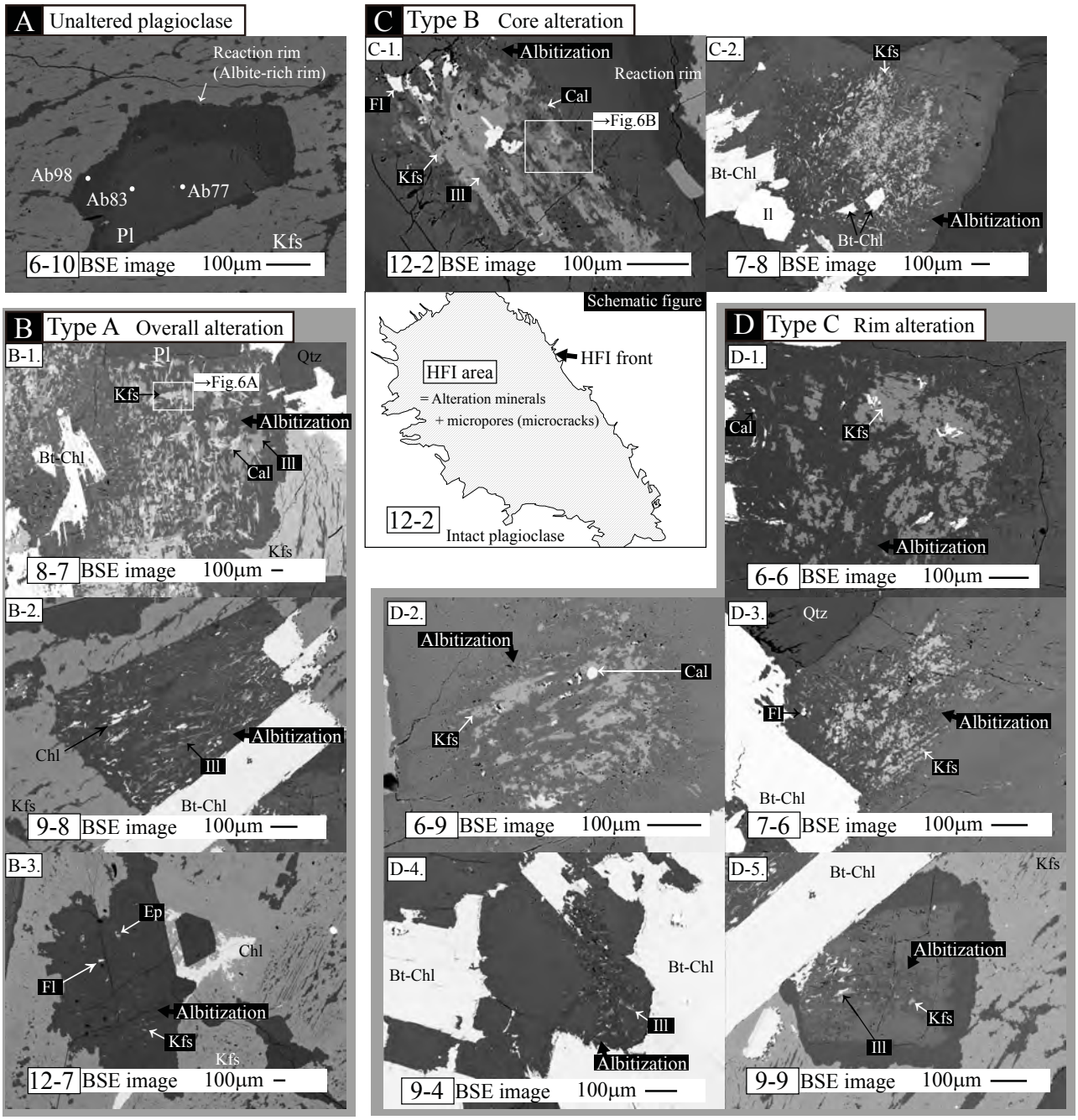

Yuguchi et al. Fig. 4

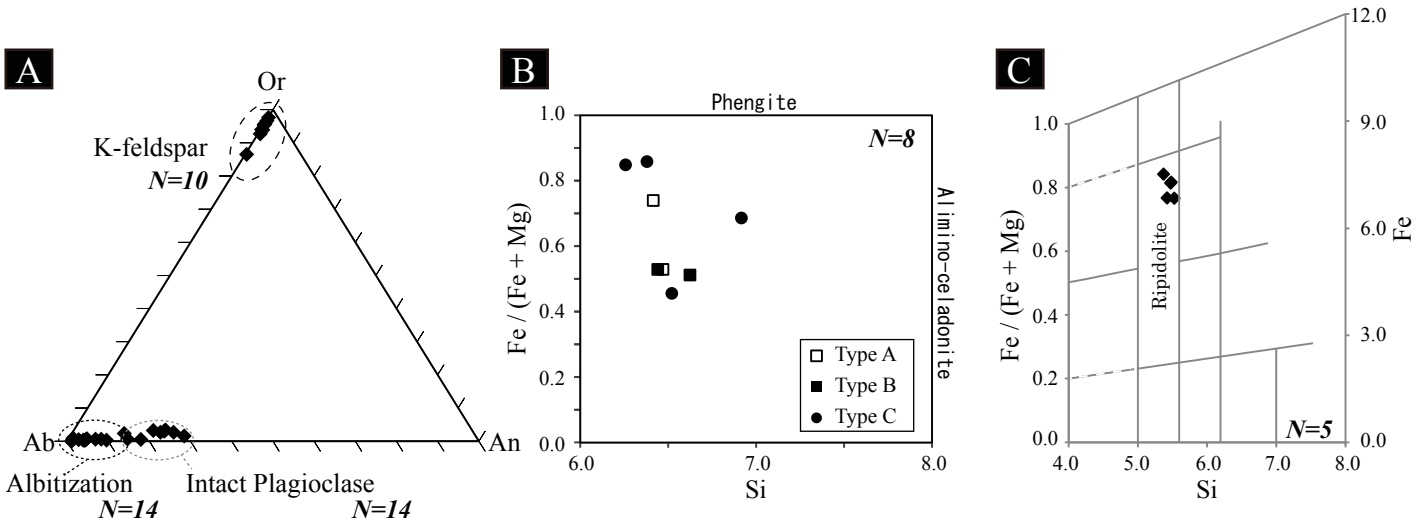

Yuguchi et al. Fig. 5

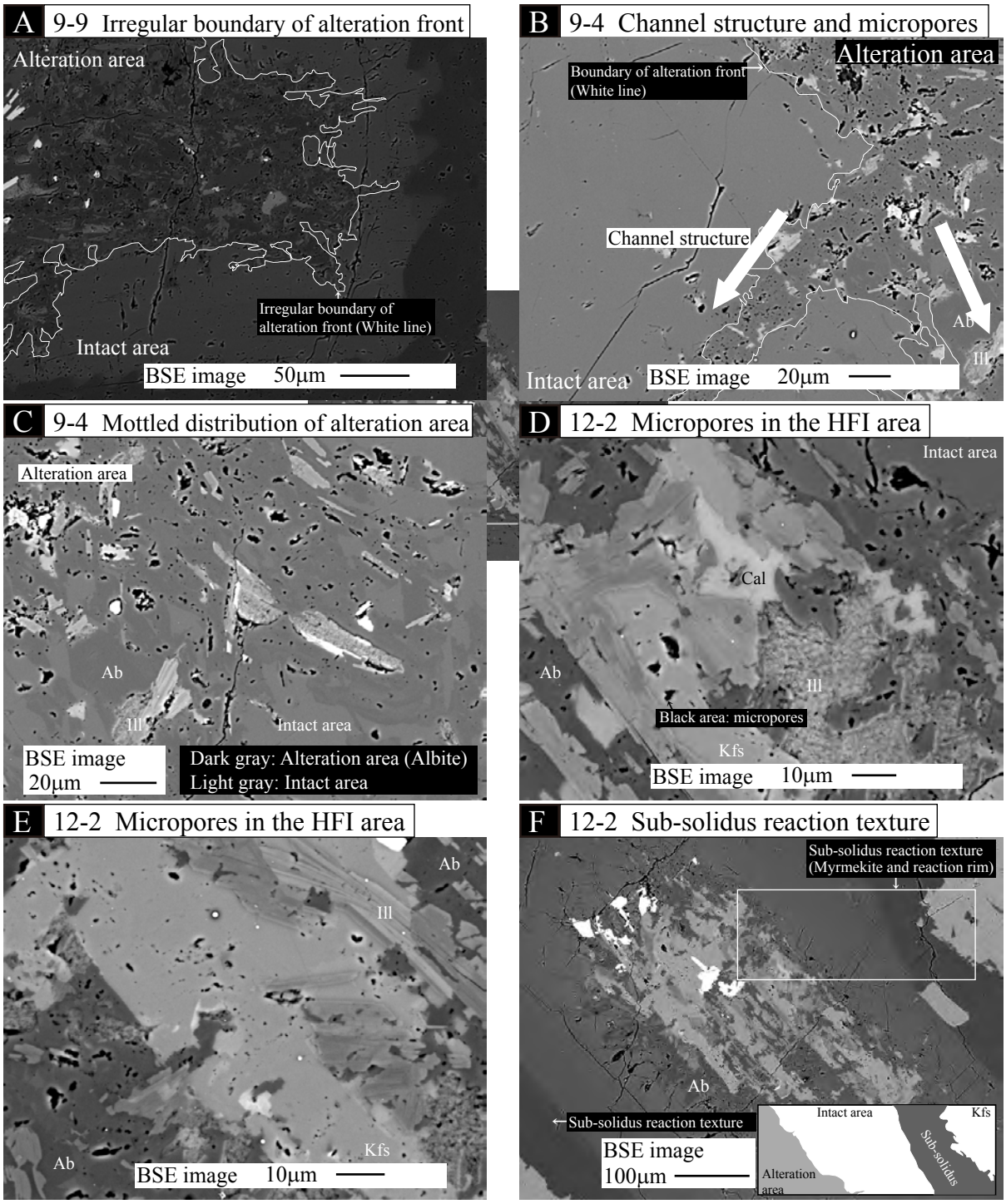

Yuguchi et al. Fig. 6

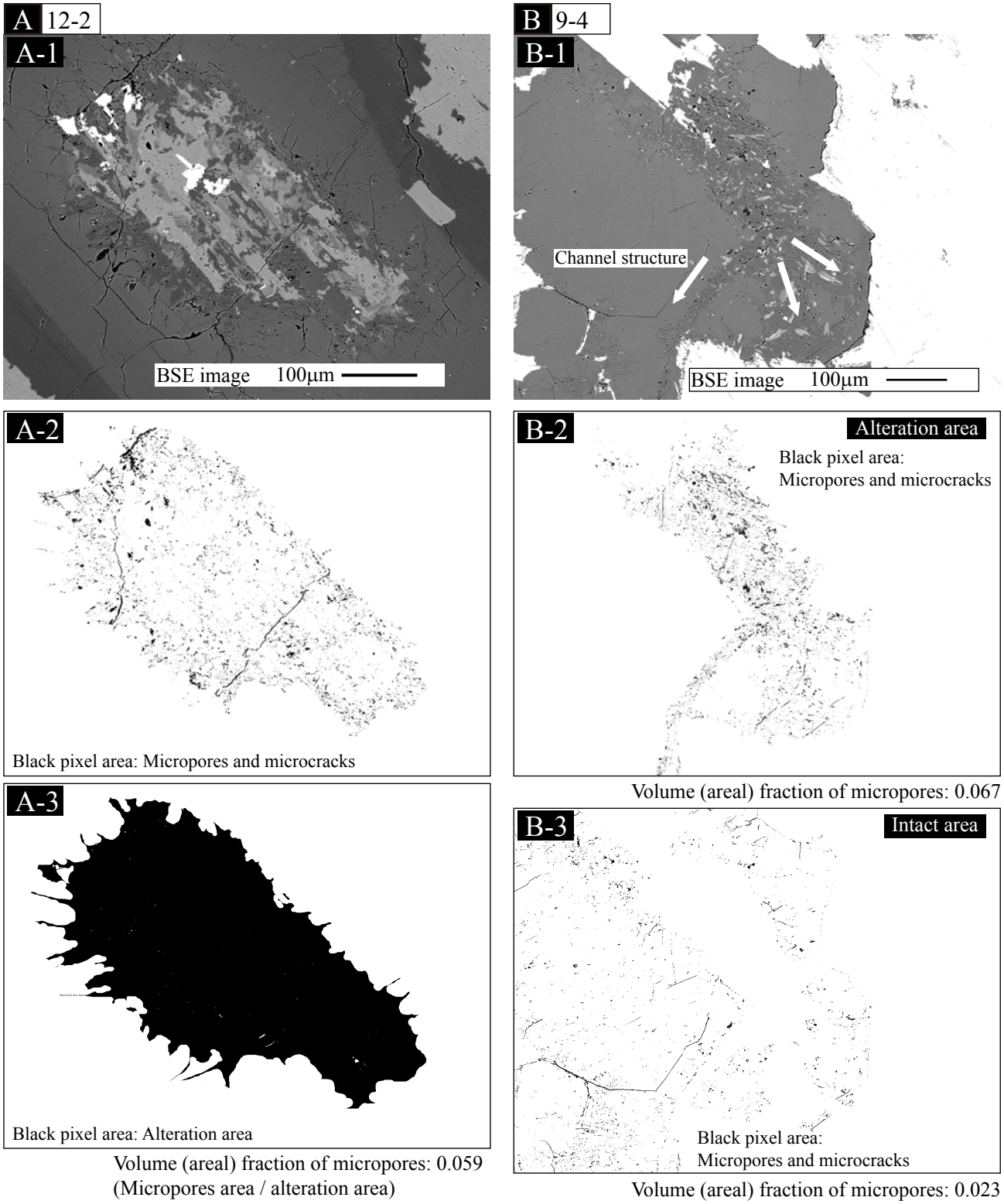

Volume (areal) fraction of micropores: 0.067

Volume (areal) fraction of micropores: 0.059
(Micropores area / alteration area)

Volume (areal) fraction of micropores: 0.023

Yuguchi et al. Fig. 7

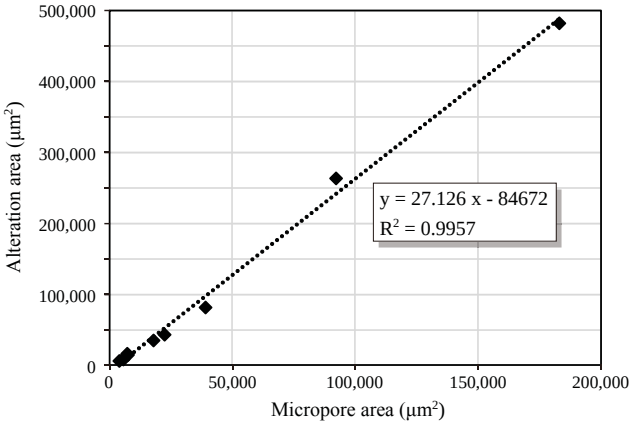

Yuguchi et al. Fig. 8

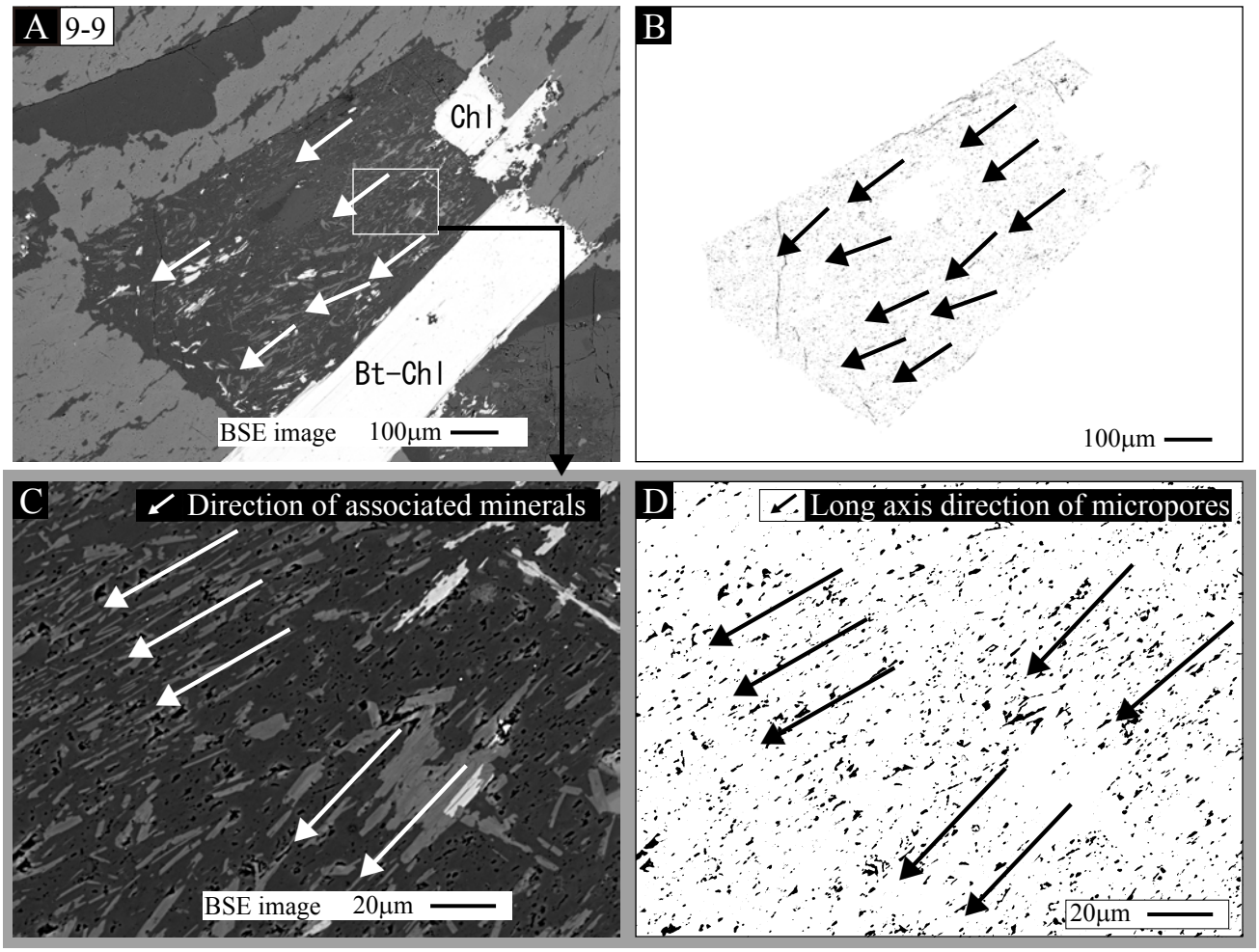

Yuguchi et al. Fig. 9

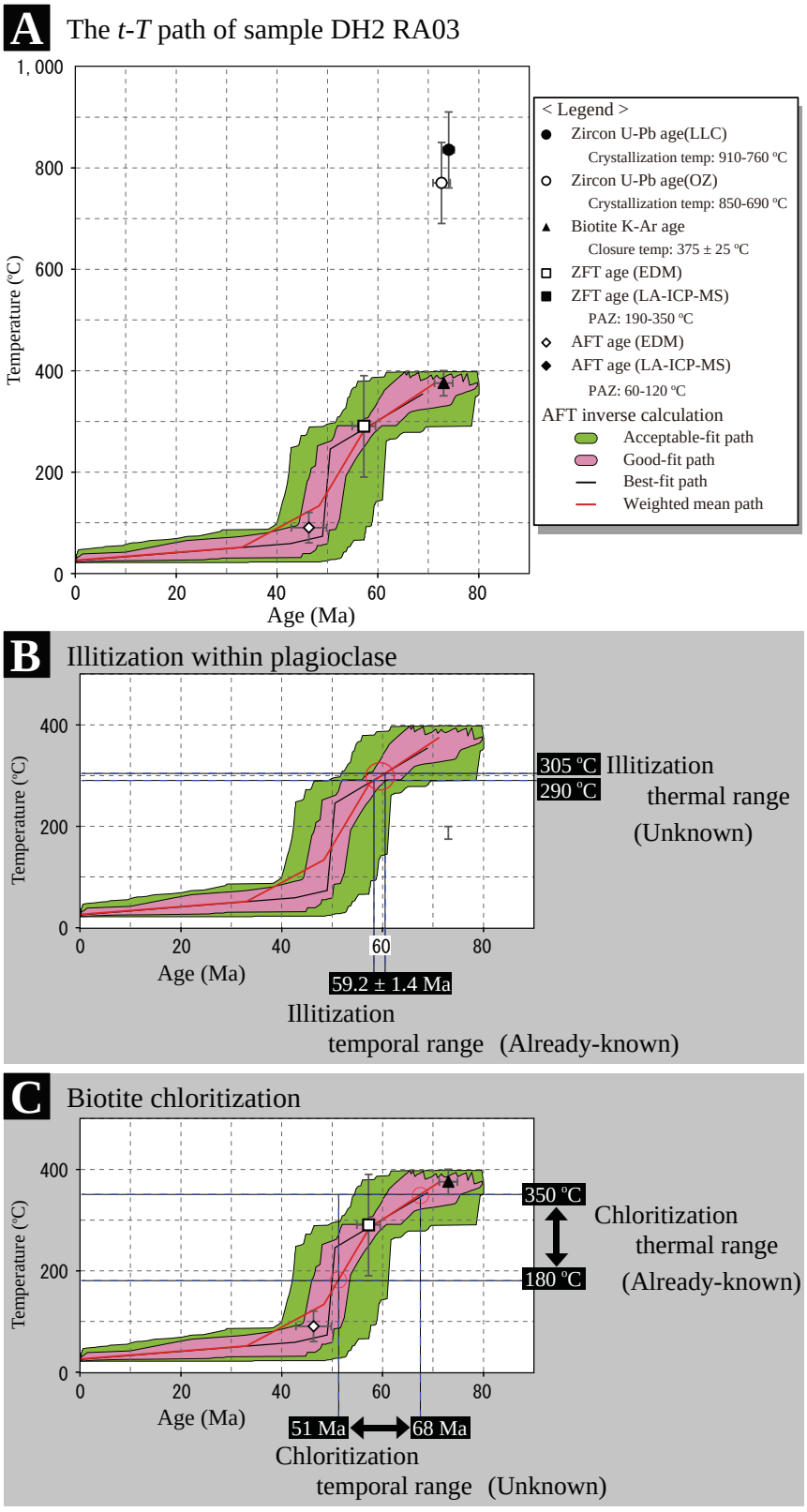

Yuguchi et al. Fig. 10

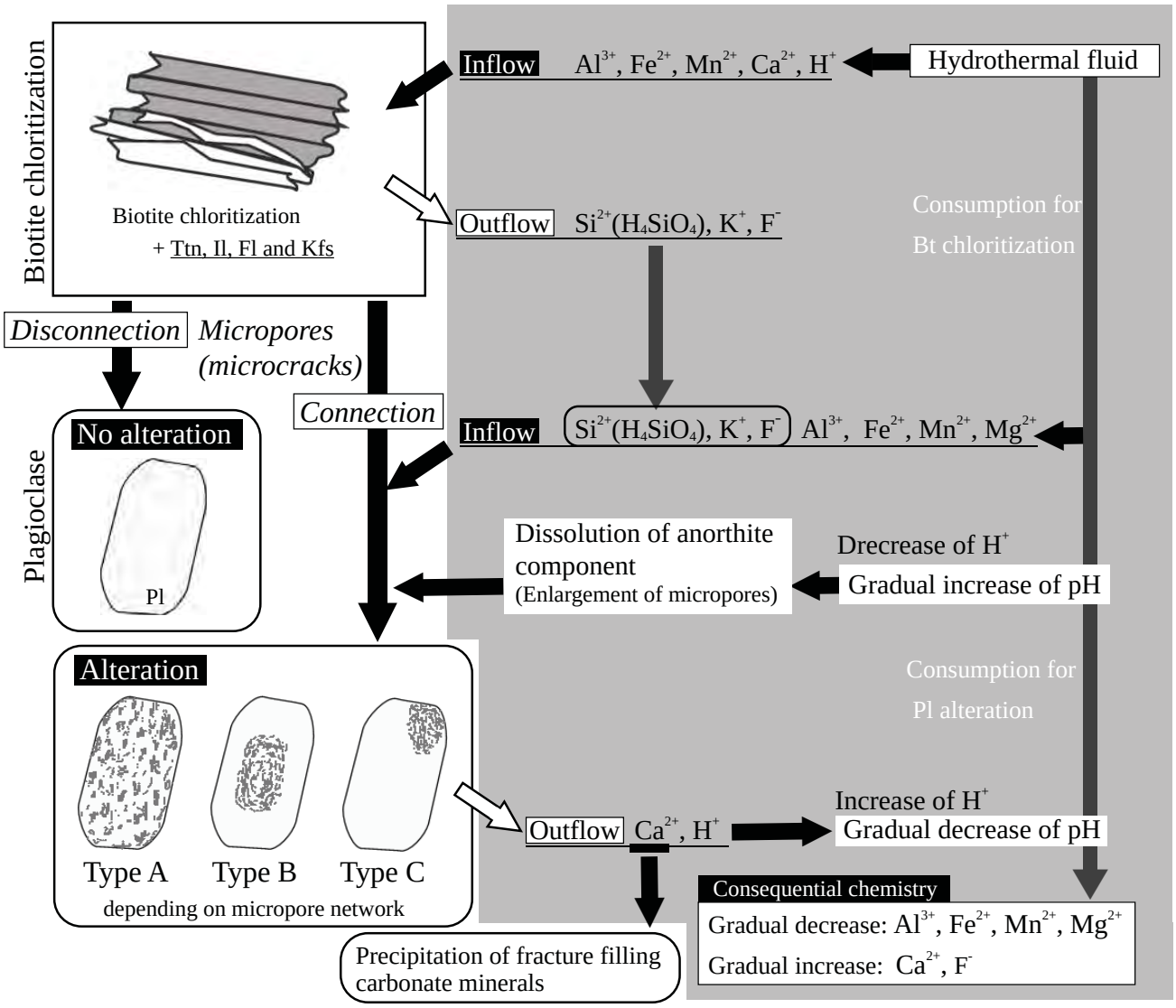

Yuguchi et al. Fig. 11

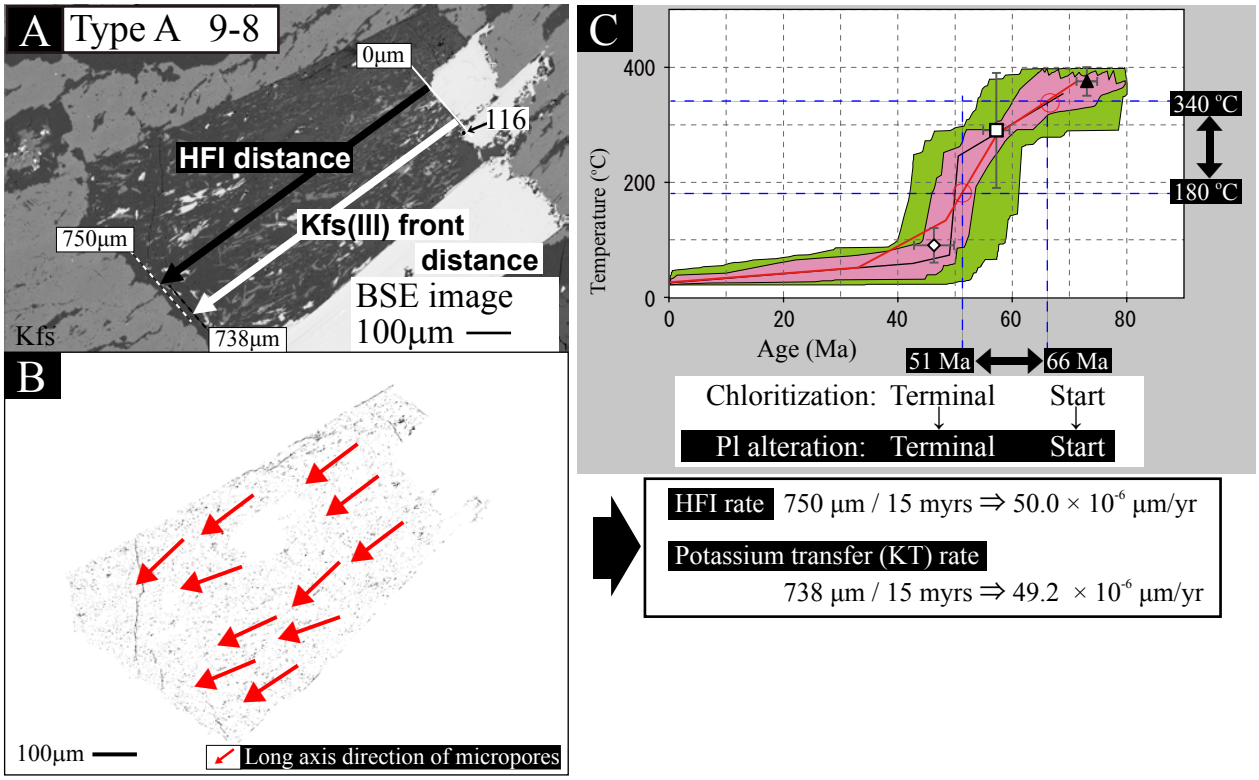

Yuguchi et al. Fig. 12

TABLE 1. Representative compositions of the reactant and products in plagioclase alteration in the Types A, B and C.

Type	Type A-1			Type A-3			Type B-1				Type B-2			
Sample No.	06MI03 314mabh 8-7			06MI03 334mabh 12-7			06MI03 334mabh 12-2				06MI03 309mabh 7-8			
Location	O11	O13	21	J05	J06	43	J09	J10	J12	J11	J07	O04	O07	J08
Mineral	**Ab**	**Kfs**	**Ill**	**Ab**	**Kfs**	**Ep**	**Pl**	**Ab**	**Kfs**	**Ill**	**Pl**	**Ab**	**Kfs**	**Ill**
(wt%)														
SiO_2	68.74	66.38	49.96	67.92	66.52	40.93	63.03	64.13	64.31	49.17	62.22	68.98	65.69	50.23
TiO_2	-	-	0.03	-	-	-	-	-	-	-	-	-	-	-
Al_2O_3	19.91	18.67	35.72	19.81	18.65	31.80	24.04	22.38	18.46	34.35	23.06	20.40	18.92	33.09
FeO	-	-	0.83	-	-	2.19	-	-	-	1.10	-	-	-	1.46
MnO	-	-	0.01	-	-	0.17	-	-	-	0.00	-	-	-	0.01
MgO	-	-	0.41	-	-	0.16	-	-	-	0.55	-	-	-	0.78
CaO	0.56	0.02	0.06	0.79	0.07	24.44	5.63	3.08	0.00	0.01	4.56	0.95	0.11	0.01
Na_2O	11.75	0.26	0.06	11.27	1.45	0.01	8.14	10.13	0.32	0.13	8.99	11.35	0.60	0.02
K_2O	0.09	16.52	8.31	0.07	14.54	0.01	0.28	0.13	16.12	10.47	0.49	0.14	15.53	8.57
F	-	-	0.11	-	-	-	-	-	-	0.35	-	-	-	0.03
Cl	-	-	0.01	-	-	-	-	-	-	-	-	-	-	0.02
Total	101.05	101.84	95.52	99.86	101.22	99.71	101.11	99.85	99.21	96.14	99.30	101.82	100.85	94.22
(atom)														
Anion	8	8	22	8	8	12.5	8	8	8	22	8	8	8	22
Si	2.98	3.01	6.47	2.97	3.01	3.07	2.76	2.83	2.99	6.44	2.78	2.96	3.00	6.62
Ti	-	-	0.00	-	-	-	-	-	-	-	-	-	-	-
Al	1.02	1.00	5.45	1.02	0.99	2.81	1.24	1.17	1.01	5.30	1.21	1.03	1.02	5.14
Fe	-	-	0.09	-	-	0.14	-	-	-	0.12	-	-	-	0.16
Mn	-	-	0.00	-	-	0.01	-	-	-	-	-	-	-	0.00
Mg	-	-	0.08	-	-	0.01	-	-	-	0.11	-	-	-	0.15
Ca	0.03	0.00	0.01	0.04	0.00	1.97	0.27	0.15	0.00	-	0.22	0.04	0.01	0.00
Na	0.99	0.02	0.02	0.96	0.13	0.00	0.69	0.87	0.03	0.03	0.78	0.95	0.05	0.01
K	0.01	0.95	1.37	0.00	0.84	0.00	0.02	0.01	0.96	1.76	0.03	0.01	0.90	1.44
F	-	-	0.04	-	-	-	-	-	-	0.14	-	-	-	0.02
Cl	-	-	0.00	-	-	-	-	-	-	-	-	-	-	0.01
Total	5.01	4.98	13.54	4.99	4.98	8.01	4.98	5.02	4.99	13.91	5.02	5.00	4.98	13.56
Ab	96.94	2.29	-	95.90	13.14	-	70.76	85.00	2.95	-	76.01	94.83	5.55	-
An	2.56	0.08	-	3.73	0.32	-	27.65	14.27	0.00	-	21.29	4.40	0.55	-
Or	0.49	97.63	-	0.38	86.53	-	1.59	0.73	97.05	-	2.70	0.78	93.90	-
V[a]	100.3	108.7	134.9	100.3	107.7	64.3	100.5	100.4	108.6	137.6	100.6	100.3	108.3	135.6

[a] Molar volume (cm^3/mol) for feldspar were calculated by propotion among albite (100.25 cm^3 / mol), anorthite (100.79 cm^3 / mol) and orthoclase (108.87 cm^3 / mol).

Molar volume for chlorite were calculated according to following equation of Parry and Downey (1982): V(chlorite) = 213.3 - 4.909 [Mg / (Mg + total Fe + Ti + Mn].

Molar volume for illite and epidote were estimated as follows: $V = (S_1m_1 + S_2m_2 + ... + S_nm_n) / D$ (Deer et al. 1974) where atomic number (S) and atomic mass (m) of element 'n' and D = mineral density. Mineral densities of illite and epidote are 3.43 and 2.75 g/cm^3, respectively, based on website of the 'Mineralogy Database (http://webmineral.com/)'.

TABLE 1. continued.

Type	Type C-1					Type C-3-1						
Sample No.	06MI03 304mabh 6-6					06MI03 309mabh 7-6						
Location	J13	54	55	J15	57	76	J21	J22	J24	J25	J23	88
Mineral	**Pl**	**Ab**	**Kfs**	**Kfs**	**Chl**	**Pl**	**Ab**	**Ab**	**Kfs**	**Kfs**	**Ill**	**Chl**
(wt%)												
SiO_2	62.50	68.48	65.11	64.77	24.08	63.85	65.83	66.29	63.94	61.53	49.61	23.94
TiO_2	-	-	-	-	0.11	-	-	-	-	-	-	-
Al_2O_3	24.02	19.59	18.11	18.45	20.92	23.50	21.01	20.74	18.09	21.15	34.44	19.47
FeO	-	-	-	-	34.77	-	-	-	-	-	0.89	36.18
MnO	-	-	-	-	2.64	-	-	-	-	-	0.03	2.01
MgO	-	-	-	-	4.42	-	-	-	-	-	0.59	6.12
CaO	5.45	0.91	0.04	0.03	0.05	4.81	2.03	1.70	0.04	0.00	0.06	0.00
Na_2O	8.94	11.52	0.44	0.45	0.05	8.93	10.75	10.82	0.35	0.36	0.09	0.00
K_2O	0.50	0.05	15.74	16.40	0.07	0.62	0.06	0.12	16.10	15.23	8.58	0.00
F	-	-	-	-	0.13	-	-	-	-	-	-	0.12
Cl	-	-	-	-	-	-	-	-	-	-	-	-
Total	101.41	100.55	99.43	100.11	87.24	101.70	99.68	99.66	98.51	98.27	94.29	87.84
(atom)												
Anion	8	8	8	8	28	8	8	8	8	8	22	28
Si	2.74	2.98	3.02	2.99	5.47	2.78	2.90	2.92	3.00	2.89	6.52	5.42
Ti	-	-	-	-	0.02	-	-	-	-	-	-	0.00
Al	1.24	1.00	0.99	1.01	5.60	1.21	1.09	1.08	1.00	1.17	5.33	5.19
Fe	-	-	-	-	6.60	-	-	-	-	-	0.10	6.85
Mn	-	-	-	-	0.51	-	-	-	-	-	0.00	0.39
Mg	-	-	-	-	1.49	-	-	-	-	-	0.12	2.06
Ca	0.26	0.04	0.00	0.00	0.01	0.22	0.10	0.08	0.00	0.00	0.01	0.00
Na	0.76	0.97	0.04	0.04	0.02	0.75	0.92	0.92	0.03	0.03	0.02	0.00
K	0.03	0.00	0.93	0.97	0.02	0.03	0.00	0.01	0.96	0.91	1.44	0.00
F	-	-	-	-	0.10	-	-	-	-	-	-	0.09
Cl	-	-	-	-	-	-	-	-	-	-	-	-
Total	5.02	5.00	4.98	5.01	19.84	5.01	5.01	5.01	5.00	5.00	13.54	20.00
Ab	72.79	95.56	4.12	3.98	-	74.42	90.25	91.41	3.16	3.50	-	-
An	24.53	4.17	0.00	0.16	-	22.19	9.40	7.93	0.18	0.00	-	-
Or	2.68	0.27	95.88	95.86	-	3.40	0.35	0.66	96.67	96.50	-	-
V[a]	100.6	100.3	108.5	108.5	212.5	100.7	100.3	100.3	108.6	108.6	135.2	212.2

TABLE 2. Mineral assemblage and the volume (areal) ratio of alteration minerals in the Types A, B and C.

Type	Sample No.	Mineral assemblage		Volume (areal) ratio of product minerals[a]
		Reactant	Products	
Type A-1	8-7	Pl	Ab, Kfs, Ill, Cal	Ab : Kfs : Ill : Cal = 1 : 0.400 : 0.451 : 0.089
Type A-2	9-8	Pl	Ab, Ill, Cal, Fl	Ab : Ill : Cal : Fl = 1 : 0.190 : 0.015 : 0.022
Type A-3	12-7	Pl	Ab, Kfs, Fl, Ep	Ab : Kfs : Fl : Ep = 1 : 0.004 : 0.002 : 0.005
Type B-1	12-2	Pl	Ab, Kfs, Ill, Cal, Fl	Ab : Kfs : Ill : Cal : Fl = 1 : 0.709 : 0.626 : 0.053 : 0.078
Type B-2	7-8	Pl	Ab, Kfs, Ill, Fl	Ab : Kfs : Ill : Fl = 1 : 0.114 : 0.218 : 0.011
Type C-1	6-6	Pl	Ab, Kfs, Cal, Fl	Ab : Kfs : Cal : Fl = 1 : 0.114 : 0.005 : 0.010
Type C-2	6-9	Pl	Ab, Kfs, Ill, Fl	Ab : Kfs : Ill : Fl = 1 : 0.129 : 0.318 : 0.017
Type C-3-1	7-6	Pl	Ab, Kfs, Ill, Cal, Fl	Ab : Kfs : Ill : Cal : Fl = 1 : 0.097 : 0.247 : 0.003 : 0.005
Type C-3-2	9-4	Pl	Ab, Kfs, Ill, Cal, Fl	Ab : Kfs : Ill : Cal : Fl = 1 : 0.042 : 0.047 : 0.019 : 0.003
Type C-3-3	9-9	Pl	Ab, Kfs, Ill, Cal, Fl	Ab : Kfs : Ill : Cal : Fl = 1 : 0.012 : 0.159 : 0.009 : 0.004

[a] The volume fraction of product minerals in the plagioclase alteration was estimated from the areal fraction of them by simply assuming the equivalence of areal and volume fractions. The area of product minerals in the plagioclase are identified by BSE images, and the areal ratio was calculated by image processing software (Scion image).

TABLE 3. Illite K-Ar dating results in the plagioclase alteration for sample No. 06MI03-8.

Sample description						**K (wt%)**	**Rad. ^{40}Ar** (10^{-8} cc STP / g) [c]	**Non-Rad. ^{40}Ar** (%)	**Age (Ma)** ± **1σ**
Borehole	Sample No.	Depth (mabh)[a]	Elevation (masl)[b]	Target mineral	Grain diameter (μm)				
06MI03	8	505.0	-304.0	Illite	0.2-2.0	3.298 ± 0.066	770.8 ± 10.0	22.1	59.2 ± 1.4

[a] Depth from the ground surface denotes meters along borehole (mabh). [b] Altitude stands for meters above sea level (masl). [c] Volume of radiogenic ^{40} argon per unit mass (1 g) under the standard temperature (0°C) and pressure (1 atm) conditions.

TABLE 4. Volume fractions of micropores in the alteration area and in the intact area.

Type	Sample No.	Area (μm^2)		Volume fractions of micropores [b]	
		Alteration area with HFI [a]	Micropores (Microcracks)	Alteration area	Intact area
No alteration	6-10	-	-	-	0.022
Type A-1	8-7	4818436	183101	0.038	-
Type A-2	9-8	355542	18133	0.051	0.045
Type A-3	12-7	2637156	92300	0.035	-
Type B-1	12-2	98182	5793	0.059	0.016
Type B-2	7-8	818539	39290	0.048	0.029
Type C-1	6-6	435801	22662	0.052	0.033
Type C-2	6-9	151167	7709	0.051	0.032
Type C-3-1	7-6	170549	7504	0.044	0.024
Type C-3-2	9-4	88314	5917	0.067	0.023
Type C-3-3	9-9	66758	4206	0.063	0.049

[a] The alteration area accompanies the hydrothermal fluid infiltration, which is defined as the area occurring the alteration minerals and micropores (and microcracks). The alteration area and micropores area were identified by BSE images and were determined by image processing software (Scion image).

[b] The volume fractions of micropores (and microcracks) in the alteration area and in the intact area were estimated from the areal fraction of them by simply assuming the equivalence of areal and volume fractions. The areal data were also taken from image analyses used by the software of Scion image.

TABLE 5. Overall reactions leading to plagioclase alteration in the Types A, B and C.

Type	Volume	Overall reaction
Type A-1 (8-7)	Constant	$Pl(Ab74) + 0.444H_4SiO_4 + 0.125CO_2 + 0.447Al^{3+} + 0.015Fe^{2+} + 0.014Mg^{2+} + 0.386K^+ + 0.007F^-$ $\rightarrow 0.517Pl(Ab97) + 0.191Kfs(Or98) + 0.172Ill + 0.125Cal + 0.197H_2O + 1.383H^+ + 0.084Ca^{2+} + 0.236Na^+$
	Reduction (3.8%)	$Pl(Ab74) + 0.321H_4SiO_4 + 0.120CO_2 + 0.384Al^{3+} + 0.015Fe^{2+} + 0.013Mg^{2+} + 0.370K^+ + 0.007F^-$ $\rightarrow 0.498Pl(Ab97) + 0.184Kfs(Or98) + 0.166Ill + 0.120Cal + 0.070H_2O + 1.146H^+ + 0.090Ca^{2+} + 0.256Na^+$
Type A-2 (9-8)	Constant	$Pl(Ab74) + 0.393H_4SiO_4 + 0.033CO_2 + 0.206Al^{3+} + 0.032Fe^{2+} + 0.011Mg^{2+} + 0.055Na^+ + 0.158K^+ + 0.148F^-$ $\rightarrow 0.818Pl(Ab98) + 0.113Ill + 0.033Cal + 0.074Fl + 0.508H_2O + 0.555H^+ + 0.109\ Ca^{2+}$
	Reduction (0.5%)	$Pl(Ab74) + 0.377H_4SiO_4 + 0.033CO_2 + 0.199Al^{3+} + 0.032Fe^{2+} + 0.011Mg^{2+} + 0.051Na^+ + 0.157K^+ + 0.147F^-$ $\rightarrow 0.814Pl(Ab98) + 0.112Ill + 0.033Cal + 0.073Fl + 0.489H_2O + 0.528H^+ + 0.109\ Ca^{2+}$
Type A-3 (12-7)	Constant	$Pl(Ab74) + 0.203H_4SiO_4 + 0.677H^+ + 0.001Fe^{2+} + 0.196Na^+ + 0.016F^-$ $\rightarrow 0.993Pl(Ab96) + 0.004Kfs(Or87) + 0.008Fl + 0.008Ep + 0.744H_2O + 0.167Al^{3+} + 0.165\ Ca^{2+} + 0.028K^+$
	Reduction (3.5%)	$Pl(Ab74) + 0.098H_4SiO_4 + 0.823H^+ + 0.001Fe^{2+} + 0.163Na^+ + 0.016F^-$ $\rightarrow 0.958Pl(Ab96) + 0.004Kfs(Or87) + 0.008Fl + 0.007Ep + 0.608H_2O + 0.204Al^{3+} + 0.167\ Ca^{2+} + 0.028K^+$
Type B-1 (12-2)	Constant	$Pl(Ab71) + 0.382H_4SiO_4 + 0.059CO_2 + 0.486Al^{3+} + 0.022Fe^{2+} + 0.020Mg^{2+} + 0.569K^+ + 0.286F^-$ $\rightarrow 0.406Pl(Ab85) + 0.266Kfs(Or97) + 0.186Ill + 0.059Cal + 0.130Fl + 0.009H_2O + 1.509H^+ + 0.023Ca^{2+} + 0.325Na^+$
	Reduction (4.3%)	$Pl(Ab71) + 0.247H_4SiO_4 + 0.056CO_2 + 0.122H_2O + 0.412Al^{3+} + 0.021Fe^{2+} + 0.019Mg^{2+} + 0.544K^+ + 0.274F^-$ $\rightarrow 0.389Pl(Ab85) + 0.255Kfs(Or97) + 0.178Ill + 0.056Cal + 0.124Fl + 1.231H^+ + 0.033Ca^{2+} + 0.341Na^+$
Type B-2 (7-8)	Constant	$Pl(Ab76) + 0.303H_4SiO_4 + 0.084H^+ + 0.035Al^{3+} + 0.010Fe^{2+} + 0.010Mg^{2+} + 0.205K^+ + 0.069F^-$ $\rightarrow 0.747Pl(Ab95) + 0.151Kfs(Or94) + 0.063Ill + 0.034Fl + 0.647H_2O + 0.151Ca^{2+} + 0.064Na^+$
	Reduction (1.9%)	$Pl(Ab76) + 0.244H_4SiO_4 + 0.175H^+ + 0.011Al^{3+} + 0.010Fe^{2+} + 0.009Mg^{2+} + 0.201K^+ + 0.067F^-$ $\rightarrow 0.732Pl(Ab95) + 0.148Kfs(Or94) + 0.062Ill + 0.033Fl + 0.576H_2O + 0.152Ca^{2+} + 0.077Na^+$
Type C-1 (6-6)	Constant	$Pl(Ab73) + 0.189H_4SiO_4 + 0.012CO_2 + 1.016H^+ + 0.107Na^+ + 0.062K^+ + 0.073F^-$ $\rightarrow 0.889Pl(Ab96) + 0.094Kfs(Or96) + 0.012Cal + 0.036Fl + 0.886H_2O + 0.257Al^{2+} + 0.170\ Ca^{2+}$
	Reduction (1.9%)	$Pl(Ab73) + 0.133H_4SiO_4 + 0.012CO_2 + 1.092H^+ + 0.090Na^+ + 0.060K^+ + 0.072F^-$ $\rightarrow 0.872Pl(Ab96) + 0.092Kfs(Or96) + 0.012Cal + 0.036Fl + 0.812H_2O + 0.275Al^{2+} + 0.172\ Ca^{2+}$
Type C-2 (6-9)	Constant	$Pl(Ab78) + 0.559H_4SiO_4 + 0.339Al^{3+} + 0.042Fe^{2+} + 0.019Mg^{2+} + 0.329K^+ + 0.121F^-$ $\rightarrow 0.685Pl(Ab95) + 0.082Kfs(Or95) + 0.158Ill + 0.048Fl + 0.626H_2O + 0.983H^+ + 0.123Ca^{2+} + 0.147Na^+$
	Reduction (1.9%)	$Pl(Ab78) + 0.495H_4SiO_4 + 0.310Al^{3+} + 0.041Fe^{2+} + 0.019Mg^{2+} + 0.322K^+ + 0.118F^-$ $\rightarrow 0.672Pl(Ab95) + 0.080Kfs(Or95) + 0.155Ill + 0.047Fl + 0.552H_2O + 0.874H^+ + 0.124Ca^{2+} + 0.160Na^+$
Type C-3-1 (7-6)	Constant	$Pl(Ab74) + 0.456H_4SiO_4 + 0.006CO_2 + 0.394Al^{3+} + 0.013Fe^{2+} + 0.016Mg^{2+} + 0.228K^+ + 0.030F^-$ $\rightarrow 0.742Pl(Ab90) + 0.067Kfs(Or97) + 0.136Ill + 0.006Cal + 0.015Fl + 0.357H_2O + 1.110H^+ + 0.131Ca^{2+} + 0.067Na^+$
	Reduction (2.0%)	$Pl(Ab74) + 0.391H_4SiO_4 + 0.006CO_2 + 0.362Al^{3+} + 0.013Fe^{2+} + 0.015Mg^{2+} + 0.223K^+ + 0.030F^-$ $\rightarrow 0.727Pl(Ab90) + 0.065Kfs(Or97) + 0.133Ill + 0.006Cal + 0.015Fl + 0.287H_2O + 0.991H^+ + 0.133Ca^{2+} + 0.081Na^+$
Type C-3-2 (9-4)	Constant	$Pl(Ab85) + 0.146H_4SiO_4 + 0.047CO_2 + 0.111H^+ + 0.007Fe^{2+} + 0.001Mg^{2+} + 0.031Na^+ + 0.059K^+ + 0.025F^-$ $\rightarrow 0.904Pl(Ab99) + 0.035Kfs(Or93) + 0.031Ill + 0.047Cal + 0.011Fl + 0.347H_2O + 0.026Al^{3+} + 0.059Ca^{2+}$
	Reduction (4.4%)	$Pl(Ab85) + 0.008H_4SiO_4 + 0.045CO_2 + 0.308H^+ + 0.006Fe^{2+} + 0.001Mg^{2+} + 0.059K^+ + 0.024F^-$ $\rightarrow 0.863Pl(Ab99) + 0.034Kfs(Or93) + 0.029Ill + 0.045Cal + 0.011Fl + 0.171H_2O + 0.075Al^{3+} + 0.062Ca^{2+} + 0.008Na^+$
Type C-3-3 (9-9)	Constant	$Pl(Ab75) + 0.387H_4SiO_4 + 0.021CO_2 + 0.224Al^{3+} + 0.004Fe^{2+} + 0.001Mn^{2+} + 0.001Mg^{2+} + 0.068Na^+ + 0.144K^+ + 0.030F^-$ $\rightarrow 0.847Pl(Ab98) + 0.009Kfs(Or96) + 0.098Ill + 0.021Cal + 0.014Fl + 0.519H_2O + 0.508H^+ + 0.180Ca^{2+}$
	Reduction (1.4%)	$Pl(Ab75) + 0.342H_4SiO_4 + 0.020CO_2 + 0.204Al^{3+} + 0.004Fe^{2+} + 0.001Mn^{2+} + 0.001Mg^{2+} + 0.056Na^+ + 0.142K^+ + 0.030F^-$ $\rightarrow 0.836Pl(Ab98) + 0.009Kfs(Or96) + 0.096Ill + 0.020Cal + 0.014Fl + 0.468H_2O + 0.434H^+ + 0.181Ca^{2+}$

TABLE 6. The calculation of reaction rate for the plagioclase alteration.

Sample	Reactant			Product			Molar variation	Albite area	Radius	Distance	Duration	Reaction rate
No.	Mineral	wt%	AP*	Mineral	wt%	AP [a]	(mols)	(cm^2)	(cm)	(cm)	(sec)	(gram atom oxygen cm^{-2} s^{-1})
9-8	Pl	63.85	76	Ab	69.96	J03	0.102	0.003	0.030	0.075	4.73E+14	1.73E-12
6-6	Pl	62.50	J13	Ab	68.48	54	0.100	0.004	0.034	0.082	3.78E+14	2.01E-12
7-6	Pl	63.85	76	Ab	66.29	J22	0.041	0.001	0.020	0.062	4.42E+14	9.25E-13
9-9	Pl	62.96	96	Ab	69.96	J32	0.116	0.001	0.013	0.038	3.15E+14	3.45E-12

[a] AP: analysis point (Table 1 and S1)